

1 **Title:**

2 **Neural correlates of individual odor preference in *Drosophila***

3

4 **Authors:**

5 Matthew A. Churgin^{1,2,*}, Danylo O. Lavrentovich^{1,2,*}, Matthew A. Smith^{1,2,10}, Ruixuan
6 Gao^{3,4,5,11}, Edward S. Boyden^{3,4,6,7,8,9}, Benjamin de Bivort^{1,2,†}

7

8 **Affiliations:**

9 ¹Organismic and Evolutionary Biology, Harvard University, Cambridge, MA 02138, USA

10 ²Center for Brain Science, Harvard University, Cambridge, MA 02138, USA

11 ³McGovern Institute, MIT, Cambridge, MA 02139, USA

12 ⁴MIT Media Lab, MIT, Cambridge, MA 02139, USA

13 ⁵Janelia Research Campus, Howard Hughes Medical Institute, Ashburn, VA 20147, USA

14 ⁶Department of Biological Engineering, MIT, Cambridge, MA 02142, USA

15 ⁷Koch Institute, Department of Biology, MIT, Cambridge, MA 02139, USA

16 ⁸Howard Hughes Medical Institute, Chevy Chase, MD 20815, USA

17 ⁹Department of Brain and Cognitive Sciences, MIT, Cambridge, MA 02139, USA

18 ¹⁰Present address: Department of Entomology, University of Wisconsin-Madison, Madison
19 WI, 53706, USA

20 ¹¹Present address: Department of Biological Sciences/Chemistry, University of Illinois
21 Chicago, Chicago, IL 60607, USA

22 *These authors contributed equally

23 †Lead Contact: debivort@oeb.harvard.edu

24 **Abstract**

25 Behavior varies even among genetically identical animals raised in the same environment.
26 However, little is known about the circuit or anatomical origins of this individuality. We show
27 individual *Drosophila* odor preferences (odor-vs-air and odor-vs-odor) are predicted by
28 idiosyncratic calcium dynamics in olfactory receptor neurons (ORNs) and projection neurons
29 (PNs), respectively. Variation in ORN presynaptic density also predicts odor-vs-odor preference.
30 The ORN-PN synapse appears to be a locus of individuality where microscale variation gives
31 rise to idiosyncratic behavior. Finally, simulating microscale stochasticity in ORN-PN synapses
32 of a 3,062 neuron model of the antennal lobe recapitulates patterns of variation in PN calcium
33 responses matching experiments. Our results demonstrate how physiological and microscale
34 structural circuit variations can give rise to individual behavior, even when genetics and
35 environment are held constant.

36

37 **Keywords:** individuality, neural circuits, sensory processing, olfaction, behavioral preference,
38 variation, *Drosophila*, antennal lobe, calcium imaging, expansion imaging

39 Introduction

40 Individuality is a fundamental aspect of behavior that is observed even among genetically-
41 identical animals reared in similar environments. We are specifically interested in individuality
42 that is evident as idiosyncratic differences in behavior that persist for much of an animal's
43 lifespan. Such variability is observed across species including round worms (Stern et al., 2017),
44 aphids (Schuett et al., 2011), fish (Laskowski et al., 2022), mice (Freund et al., 2013), and people
45 (Johnson et al., 2010). Small, genetically tractable model species, such as *Drosophila*, are
46 particularly promising for discovering the genetic and neural circuit basis of individual behavior
47 variation. Flies exhibit individuality in many behaviors (Werkhoven et al., 2021), and the
48 mechanistic origins of this variation has been studied for phototactic preference (Kain et al.,
49 2012), temperature preference (Kain et al., 2015), locomotor handedness (Ayroles et al., 2015;
50 Buchanan et al., 2015; de Bivort et al., 2022), object-fixated walking (Linneweber et al., 2020),
51 and odor preference (Honegger et al., 2019). Generally, the neural substrates of individuality are
52 poorly understood, though in a small number of instances nanoscale circuit correlates of
53 individual behavioral biases have been identified (Linneweber et al., 2020; Skutt-Kakaria et al.,
54 2019). We hypothesize that as sensory cues are encoded and transformed to produce motor
55 outputs, their representation in the nervous system becomes increasingly idiosyncratic and
56 predictive of individual behavioral responses. We seek to identify “loci of individuality” – sites
57 at which this idiosyncrasy emerges.

58
59 Olfaction in the fruit fly *Drosophila melanogaster* is an amenable sensory system for identifying
60 loci of individuality, as 1) individual odor preferences can be recorded readily, 2) neural
61 representations of odors can be measured via calcium imaging, 3) the circuit elements of the
62 pathway are well-established, and 4) a deep genetic toolkit enables mechanism-probing
63 experiments. The neuroanatomy of the olfactory system, from the antenna through its first
64 central-brain processing neuropil, the antennal lobe (AL), is broadly stereotyped across
65 individuals (Couto et al., 2005; Grabe et al., 2015; Wilson et al., 2004). The AL features ~50
66 anatomically identifiable microcircuits called glomeruli (Figure 1A). Each glomerulus represents
67 an odor-coding channel and receives axon inputs from olfactory receptor neurons (ORNs)
68 expressing the same olfactory receptor gene (de Bruyne et al., 2001). Uniglomerular projection
69 neurons (PNs) carry odor information from each glomerulus deeper into the brain (Jeanne and
70 Wilson, 2015). AL-intrinsic local neurons (LNs) project among glomeruli (Chou et al., 2010)
71 and modulate odor representations (Wilson and Laurent, 2005). Glomerular organization is a key
72 stereotype of the AL; using glomeruli as landmarks, one can identify comparable ORN axons
73 and PNs across individuals.

74
75 Several possible determinants of individual odor preference can already be hypothesized for the
76 fly olfactory circuit (Rihani and Sachse, 2022). Individual flies differ in their PN calcium
77 responses to identical odor stimuli, as well as their odor-vs-odor preference choices (Honegger et
78 al., 2019). The extent of preference variability depends on dopamine and serotonergic

79 modulation (Honegger et al., 2019). Neuromodulation clearly plays a role in the regulation of
80 behavioral individuality (Maloney, 2021), but its effects vary by modulator and behavior (de
81 Bivort et al., 2022; Kain et al., 2012). With respect to wiring variation, the number of ORNs and
82 PNs innervating a given glomerulus varies within hemispheres (Tobin et al., 2017) and across
83 individuals (Grabe et al., 2016; Schlegel et al., 2020), as does the glomerulus-innervation pattern
84 of individual LNs (Chou et al., 2010). Subpopulations of LNs and PNs express variable serotonin
85 receptors (Sizemore and Dacks, 2016), so the effects of neuromodulation and wiring may
86 interact to influence individuality. Little is known about possible molecular or nanoscale
87 correlates of individual behavioral bias. Thus, individual odor preference could have its origins
88 in many potential mechanisms, ranging from circuit wiring to modulation to neuronal intrinsic
89 properties.

90
91 Outside the olfactory system, there are two instances in which microscale circuit variation is
92 known to predict individual behavioral preference. Wiring asymmetry in an individual fly's
93 dorsal cluster neurons is predictive of the straightness of its object-oriented walking behavior
94 (Linneweber et al., 2020), and left-right asymmetry in the density of presynaptic sites of
95 protocerebral bridge - lateral accessory lobe-projecting neurons predicts an individual fly's
96 idiosyncratic turning bias (Skutt-Kakaria et al., 2019).

97
98 In this work, we sought to identify loci of individuality by measuring odor preferences and
99 neural responses to odors in the same individuals and asking whether the latter predicted the
100 former. We found that idiosyncratic calcium responses in specific neurons were predictive of
101 olfactory preferences – variation in ORN responses predicts odor-vs-air preference; variation in
102 PN responses predicts odor-vs-odor preference. Zooming into a molecular component, variation
103 in the scaffolding protein Bruchpilot in ORN presynaptic terminals is also predictive of odor
104 preference variation. To unify these results and connect wiring variation to circuit outputs, we
105 simulated developmental variation in a 3,062-neuron spiking model of the antennal lobe.
106 Simulated stochasticity in the ORN-PN synapse recapitulated our empirical findings. Thus, we
107 identified the ORN-PN synapse as a locus of individuality in fly odor preference, demonstrating
108 that behaviorally-relevant variation in neural circuits can be found in the sensory periphery at the
109 nanoscale.

110 111 **Results**

112 *Individual flies encode odors idiosyncratically*

113 Focusing on behavioral variation within a genotype, we used isogenic animals expressing the
114 fluorescent calcium reporter GCamp6m (Chen et al., 2013) in either of the two most peripheral
115 neural subpopulations of the *Drosophila* olfactory circuit, ORNs or PNs (Figure 1E). We
116 performed head-fixed 2-photon calcium imaging after measuring odor preference in an
117 untethered assay (Honegger et al., 2019) (Figure 1B-D, Figure 1 – figure supplement 1A).

118 Individual odor preferences are stable over timescales longer than this experiment (Figure 1 –
119 figure supplement 1B-E).

120

121 We measured volumetric calcium responses in the antennal lobe (AL), where ORNs synapse
122 onto PNs in ~50 discrete microcircuits called glomeruli (Figure 1A) (Couto et al., 2005; Grabe et
123 al., 2015). Flies were stimulated with a panel of 12 odors plus air (Figure 1D, Figure 1 – figure
124 supplement 2) and *k*-means clustering was used to automatically segment the voxels of 5
125 glomeruli from the resulting 4-D calcium image stacks (Figure 1E, Figure 1 – figure supplement
126 4, Materials and Methods) (Couto et al., 2005). Both ORN and PN odor responses were roughly
127 stereotyped across individuals (Figure 1G,H), but also idiosyncratic (Honegger et al., 2019).
128 Responses in PNs appeared to be more idiosyncratic than ORNs (Figure 1J); a logistic linear
129 classifier decoding fly identity from glomerular responses was more accurate when trained on
130 PN than ORN responses (Figure 1 – figure supplement 5A). While the responses of single ORNs
131 are known to vary more than those of single PNs (Wilson, 2013), our recordings represent the
132 total response of all ORNs or PNs in a glomerulus. This might explain our observation that
133 ORNs exhibited less idiosyncrasy than PNs. PN responses were more variable within flies, as
134 measured across the left and right hemisphere ALs, compared to ORN responses (Figure 1 –
135 figure supplement 5C), consistent with the hypothesis that odor representations become more
136 idiosyncratic farther from the sensory periphery.

137

138 *Individual ORN responses predict odor-air preference*

139 Next we analyzed the relationship of idiosyncratic coding to odor preference, by asking in which
140 neurons (if any) did calcium responses predict individual preferences of flies choosing between
141 air and an aversive odor (3-octanol, OCT; Figure 1 – figure supplement 1B; Supplementary
142 Video 1). Because we could potentially predict preference (a single value) using numerous
143 glomerular-odor predictors, and had a limited number of observations (dozens), we used
144 dimensional reduction to make parsimonious predictions. We computed the principal
145 components (PCs) of the glomerulus-odor responses (in either ORNs or PNs) across individuals
146 (Figure 1G-I; Figure 1 – figure supplement 3, Figure 1 – figure supplement 7) and fit linear
147 models to predict the behavior of individual flies from their values on the odor response PCs. PC
148 1 of ORN activity was a significant predictor of odor preference ($r = 0.48$; $p = 0.0099$; Figure
149 1K,L). PC 1 of PN activity was also correlated with odor preference in separate model training
150 and testing experiments (Figure 2 – figure supplement 1; statistics from combined train and test
151 data: $r = 0.29$, $p = 0.035$, Figure 1K,M). Our interpretation is that ORN responses are
152 idiosyncratic and predict individual odor-vs-air preference, and that these idiosyncrasies are
153 transmitted to PNs, where they remain predictive of behavioral responses.

154

155 How should we interpret the calcium PCs only predicting odor preference with $r = \sim 0.4$? This
156 value falls short of 1.0 due to at least two factors: 1) any non-linearity in the relationship between
157 calcium responses and behavior, and 2) sampling error in, and temporal instability of, behavior

158 and calcium responses over the duration of the experiment. A lower bound on the latter can be
159 estimated from the repeatability of behavioral measures over time (Figure 1 – figure supplement
160 1B-E). To disentangle these effects, we performed a statistical analysis that estimated model
161 performance in the absence of sampling error and drift in the measurement of behavior and
162 calcium responses, i.e., the strength of the linear relationship between latent behavior and
163 calcium states (Figure 4 – figure supplement 1; Materials and Methods). This analysis implies
164 the nominal correlation of 0.48 between behavior and PC1 of ORN calcium responses
165 corresponds to a correlation between latent calcium and behavior states (ρ_{signal}) of 0.64. This
166 makes intuitive sense because the raw model R^2 (0.23) is close to the behavior repeatability R^2
167 (0.27), an upper-limit on model performance (Figure 1 – figure supplement 1B). The model
168 predicting odor-vs-air behavior from PC1 of PN calcium responses has an estimated ρ_{signal} of
169 0.40 (Figure 4).

170

171 *PN, but not ORN, responses predict odor-odor preference*

172 Variation in the sensory periphery has been previously implicated as a driver of behavioral
173 variation (Michelson et al., 2017; Osborne et al., 2005), but we wondered whether ORNs would
174 be a locus of individuality for a behavior requiring the comparison of two odors (rather than just
175 the sensation of a single odor). So we next determined if idiosyncratic calcium responses could
176 predict individual preferences in an odor-vs-odor choice (Figure 1 – figure supplement 1D,E;
177 (Honegger et al., 2019); Supplementary Video 2), specifically between the aversive
178 monomolecular odorants (OCT) and 4-methylcyclohexanol (MCH). We assessed if any of the
179 first 5 PCs of PN calcium responses was a linear predictor of individual odor-vs-odor
180 preferences. PC 2 accounted for 15% of preference variance in a training set of 47 flies (Figure 2
181 – figure supplement 1C). This PC 2-based model explained 31% of preference variance on test
182 data (n=22 flies) (Figure 2 – figure supplement 1D). Combined train/test statistics ($r = 0.45$; $p =$
183 0.0001) are presented in Figure 1N,P. We estimate that the correlation between between latent
184 PN calcium and odor-vs-odor behavioral states is $\rho_{signal} = 0.75$ (Figure 4).

185

186 No PCs of ORN neural activity could linearly predict odor preference beyond the level of
187 shuffled controls (n=35 flies) (Figure 1N,O; Figure 4). The best ORN PC model only predicted
188 odor-vs-odor behavior with a nominal R^2 of 0.031 ($\rho_{signal} = 0.30$). Projecting ORN data onto PC
189 2 of PN responses (the successful model) did not predict odor-vs-odor behavior ($R^2=0.060$).
190 Therefore, whereas idiosyncratic ORN responses (and PN responses) were predictive of odor-vs-
191 air preferences, only PN responses were predictive of odor-vs-odor preferences.

192

193 We next sought an intuitive understanding of the models linking calcium responses and odor
194 preference. The loadings of the ORN and PN PCs indicate that variation across individuals was
195 correlated at the level of glomeruli much more strongly than odorant (Figure 1 – figure
196 supplements 3, 7). This suggests that stochastic variation in the olfactory circuit results in
197 individual-level fluctuations in the responses of glomeruli-specific rather than odor-specific

198 responses. In the case of the odor-vs-air model, the PC 1 loadings of both ORN and PN neural
199 activity were non-negative across all glomerulus-odor response dimensions (Figure 2A,D),
200 apparently representing each individual's total response in all glomerulus-odorant combinations.
201 Indeed, a linear model that simply sums all calcium responses in ORNs (Figure 2B,E) predicted
202 behavior with $R^2=0.25$ ($\rho_{signal} = 0.67$); for PN responses, it was somewhat predictive, though less
203 so ($R^2=0.098$; $\rho_{signal} = 0.43$). For both ORNs and PNs, the model's slope parameter (β) was
204 negative (Table 1), meaning that stronger AL responses correlated with stronger preference for
205 air, consistent with OCT being aversive. Thus, flies whose ORNs and PNs respond, as a
206 population, more strongly to OCT are more likely to avoid it.

207
208 In the odor-vs-odor preference model, the loadings of PC2 of PN calcium responses contrast the
209 responses of the DM2 and DC2 glomeruli with opposing weights (Figure 2G), suggesting that
210 the activation of DM2 relative to DC2 predicts the likelihood of a fly preferring OCT to MCH.
211 Indeed, a linear model constructed from the total DM2 minus total DC2 PN response (Figure 2H)
212 predicted individual preference for OCT versus MCH ($R^2=0.12$; $\rho_{signal} = 0.59$; Figure 2I). The
213 model beta coefficient was negative (Table 1), indicating that greater activation of DM2 vs DC2
214 correlates with preference for MCH. With respect to odor-vs-odor behavior, we conclude that the
215 relative responses of DM2 vs DC2 in PNs largely explains an individual's preference.

216
217 Odor experience has been shown to modulate subsequent AL responses (Golovin and Broadie,
218 2016; Iyengar et al., 2010; Sachse et al., 2007). This raises the possibility that our models were
219 actually predicting individual flies' past odor experiences (i.e., the specific pattern of odor
220 stimulation flies received in the behavioral assay) rather than their preferences. To address this,
221 we imposed the specific odor experiences of previously tracked untethered flies (in the odor-vs-
222 odor assay) on naive "yoked" control flies (Figure 2J) and measured PN odor responses of the
223 yoked flies. Applying the PN PC 2 model to the yoked calcium responses did not predict flies'
224 odor experience ($R^2=0.019$; Figure 2K). Thus, the responses of DM2 vs DC2 in PNs do not
225 predict individual open-loop odor experiences.

226
227 Previous work found that PN response transients, rather than fixed points, contain more odor
228 identity information (Mazor and Laurent, 2005). We therefore asked at which times during odor
229 presentation an individual's neural responses could best predict odor preference. Applying each
230 of our three successful calcium-to-behavior models (ORN PC1-odor-vs-air, PN PC1-odor-vs-air,
231 PN PC2-odor-vs-odor) to the time-varying calcium signals, we found that in all cases, behavior
232 prediction generally rose during odor delivery (Figure 4 – figure supplement 2A-C). In ORNs,
233 the predictive accuracy remained high after odor offset, whereas in PNs it declined. Thus, the
234 overall sensitivity of ORNs that appears to predict odor-vs-air preferences may persist after odor
235 stimulation ends. The times during which calcium responses predicted individual behavior
236 generally aligned to the times during which a linear classifier could decode odor identity from

237 ORN or PN responses (Figure 4 – figure supplement 2D), suggesting that idiosyncrasies in odor
238 encoding predict individual preferences.

239

240 *Variation in a presynaptic scaffolding protein predicts odor-odor preference variation*

241 We next investigated how structural variation in the nervous system might underlie the variations
242 in neural activity that correlate with idiosyncratic behavior. Because PN, but not ORN, calcium
243 responses predicted odor-vs-odor preference, we hypothesized that a circuit element between
244 ORNs to PNs could confer onto PNs behaviorally-relevant physiological idiosyncrasies absent in
245 ORNs. We therefore imaged presynaptic T-bar density in ORNs using transgenic mStrawberry-
246 tagged Brp-Short, immunohistochemistry and confocal microscopy (Mosca and Luo, 2014) after
247 measuring individual preference for OCT versus MCH (Figure 3A). Brp-Short density was
248 quantified as fluorescence intensity / glomerulus volume for 4 of the 5 focus glomeruli (Figure
249 3B, Figure 3 – figure supplement 1A-F; DL5 was not readily segmentable across samples, but
250 was dispensable in all behavior-predicting models). This measure was consistent across
251 hemispheres (Figure 3 – figure supplement 1C), while also showing variation among individuals.

252

253 To begin assessing the relationship between presynaptic structural variation and behavior, we
254 calculated the principal components of Brp-Short density across individuals. PCs 1 and 2 were
255 qualitatively similar to those in our calcium imaging experiments: PC 1 was non-negative
256 positive across glomeruli, reflecting global average staining intensity, and PC 2 exhibited a sign
257 contrast between DC2 loadings and all other glomerulus loadings (Figure 3 – figure supplement
258 1G). As in the PN calcium response models, PC 2 of Brp-Short density was the best predictor of
259 odor-vs-odor preferences in training data (Figure 3D-E, Figure 3 – figure supplement 1I, $R^2 =$
260 0.22 , $n=22$ flies) and for test data (Figure 3 – figure supplement 1J, $R^2 = 0.078$, $n=31$ flies;
261 statistics from combined train and test data: $R^2 = 0.088$, $n=53$ flies, Figure 3F). We tested our
262 intuitive hypothesis that PC 2 captures the differential response of DM2 vs DC2 by applying the
263 “DM2 minus DC2 model” (Figure 2H) to the Brp-Short data (Figure 3G). While this
264 rudimentary model did not attain statistical significance, it had a negative beta coefficient,
265 implying that higher presynaptic density in DM2 compared to DC2 correlates with preference for
266 MCH (Table 1), consistent with the beta parameter of the PN calcium response model.

267

268 The range of differences between DM2 and DC2 Brp-Short staining across individuals (-50% to
269 40%; normalized by the average of the two glomeruli) was less than that of PN calcium response
270 differences (-60% to 100%; Figure 3 – figure supplement 2), suggesting that presynaptic density
271 variation is not the full explanation of calcium response variability. Consistently, the best
272 presynaptic density models are less predictive of behavior than the best calcium response models
273 ($R^2=0.088$ vs $R^2=0.22$; $\rho_{signal} = 0.51$ and 0.75 , respectively; Figure 2 – figure supplement 1C,D
274 vs Figure 3 – figure supplement 1I,J). Nevertheless, differences in presynaptic inputs to DM2
275 and DC2 PNs may contribute to variation in DM2 and DC2 calcium dynamics, in turn giving rise
276 to individual preferences for OCT versus MCH.

277

278 To help formulate hypotheses about what variable Brp-Short staining represented on a
279 microstructural level, we performed paired behavior and expansion microscopy (Asano et al.,
280 2018; Gao et al., 2019) in flies expressing Brp-Short specifically in DC2-projecting ORNs
281 (Supplementary Video 3). Expansion yielded a ~4-fold increase in linear resolution, allowing
282 imaging of individual Brp-Short puncta (Figure 3 – figure supplement 1K) (Gao et al., 2019).
283 While the sample size (n=8) of this imaging pipeline did not warrant a formal modeling analysis,
284 the trend between density of Brp-Short in DC2 and odor-vs-odor preference was more consistent
285 with a positive correlation than the trend between Brp-Short volume and odor-vs-odor preference
286 (Figure 3 – figure supplement L,M). These results hint that variation in the density of Bruchpilot
287 protein within presynaptic sites, rather than other biophysical properties, may be a critical factor
288 underlying physiological and behavioral individuality.

289

290 *Developmental stochasticity in a simulated AL recapitulates empirical PN response variation*
291 Finally, we sought an integrative understanding of how synaptic variation plays out across the
292 olfactory circuit to produce behaviorally-relevant physiological variation. We developed a leaky-
293 integrate-and-fire model of the entire AL, comprising 3,062 spiking neurons and synaptic
294 connectivity taken directly from the *Drosophila* hemibrain connectome (Scheffer et al., 2020).
295 After tuning the model to perform canonical AL computations, we introduced different kinds of
296 stochastic variations to the circuit and determined which (if any) would produce the patterns of
297 idiosyncratic PN response variation observed in our calcium imaging experiments (Figure 5A).
298 This approach assesses potential mechanisms linking developmental variation in synapses to
299 physiological variation that apparently drives behavioral individuality.

300

301 The biophysical properties of neurons in our model (Figure 5B, Table 2) were determined by
302 published electrophysiological studies (See *Voltage model* in Materials and Methods) and were
303 similar to those used in previous fly models (Kakaria and de Bivort, 2017; Pisokas et al., 2020).
304 The polarity of neurons was determined largely by their cell type (ORNs are excitatory, PNs
305 predominantly excitatory, and LNs predominantly inhibitory – explained further in Materials and
306 Methods). The strength of synaptic connections between any pair of AL neurons was given by
307 the hemibrain connectome (Scheffer et al., 2020) (Figure 5C). Odor inputs were simulated by
308 injecting current into ORNs to produce spikes in those neurons at rates that match published
309 ORN-odor recordings (Münch and Galizia, 2016), and the output of the system was recorded as
310 the firing rates of PNs during odor stimulation (Figure 5D). At this point, there remained only
311 four free parameters in our model, the relative sensitivity (postsynaptic current per upstream
312 action potential) of each AL cell type (ORNs, PNs, excitatory LNs and inhibitory LNs). We
313 explored this parameter space manually, and identified a configuration in which AL simulation
314 (Figure 5 – figure supplement 1) recapitulated four canonical properties seen experimentally
315 (Figure 5 – figure supplement 2): 1) typical firing rates at baseline and during odor stimulation
316 (Bhandawat et al., 2007; Dubin and Harris, 1997; Jeanne and Wilson, 2015; Seki et al., 2010), 2)

317 a more uniform distribution of PN firing rates compared to ORN rates (Bhandawat et al., 2007),
318 3) greater separation of PN odor representations compared to ORN representations (Bhandawat
319 et al., 2007), and 4) a sub-linear transfer function between ORNs and PNs (Bhandawat et al.,
320 2007). Thus, our simulated AL appeared to perform the fundamental computations of real ALs,
321 providing a baseline for assessing the effects of idiosyncratic variation.

322
323 We simulated stochastic individuality in the AL circuit in two ways (Figure 5E): 1) glomerular-
324 level variation in PN input-synapse density (reflecting a statistical relationship observed between
325 glomerular volume and synapse density in the hemibrain, Figure 5 – figure supplement 4), and 2)
326 bootstrapping of neuronal compositions within cell types (reflecting variety in developmental
327 program outcomes for ORNs, PNs, etc.). Supplementary Video 4 shows the diverse connectivity
328 matrices attained under these resampling approaches. We simulated odor responses in thousands
329 of ALs made idiosyncratic by these sources of variation, and in each, recorded the firing rates of
330 PNs when stimulated by the 12 odors from our experimental panel (Figure 5F, Figure 5 – figure
331 supplement 1).

332
333 To determine which sources of variation produced patterns of PN coding variation consistent
334 with our empirical measurements, we compared principal components of PN responses from real
335 idiosyncratic flies to those of simulated idiosyncratic ALs. Empirical PN responses are strongly
336 correlated at the level of glomeruli (Figure 5G; Figure 1 – figure supplement 7). As a positive
337 control that the model can recapitulate this empirical structure, resampling PN input-synapse
338 density across glomeruli produced PN response correlations strongly organized by glomerulus
339 (Figure 5I). As a negative control, variation in PN responses due solely to poisson timing of
340 ORN input spikes (i.e., absent any circuit idiosyncrasy) was not organized at the glomerular level
341 (Figure 5H). Strikingly, bootstrapping ORN membership yielded a strong glomerular
342 organization in PN responses (Figure 5J). The loadings of the top PCs under ORN bootstrapping
343 are dominated by responses of a single glomerulus to all odors, including DM2 and DC2. This is
344 reminiscent of PC2 of PN calcium responses, with prominent (opposite sign) loadings for DM2
345 and DC2. Bootstrapping LNs, in contrast, produced much less glomerular organization (Figure
346 5K), with little resemblance to the loadings of the empirical calcium PCs. The PCA loadings for
347 simulated PN responses under all combinations of cell type bootstrapping and PN input-synapse
348 density resampling are given in Figure 5 – figure supplement 5.

349
350 DM2 and DC2 (also DL5) stand out in the PCA loadings under PN input-synapse density
351 resampling and ORN bootstrapping (Figure 5I,J), suggesting that behaviorally-relevant PN
352 coding variation is recapitulated in this modeling framework. To formalize this analysis, for each
353 idiosyncratic AL, we computed a “behavioral preference” by applying the PN PC2 linear model
354 (Figure 1N,P) to simulated PN responses. We then determined how accurately a linear classifier
355 could distinguish OCT- vs MCH-preferring ALs in the space of the first 3 PCs of PN responses
356 (Figure 5 – figure supplement 6). High accuracy was attained under PN input-synapse density

357 resampling and ORN bootstrapping (sources of circuit variation that produced PN response
358 loadings highlighting DM2 and DC2). Thus, developmental variability in ORN populations may
359 drive patterns of PN physiological variation that in turn drive individuality in odor-vs-odor
360 choice behavior.

361

362

363 **Discussion**

364 We found elements of the *Drosophila* olfactory circuit where patterns of physiological activity
365 emerge that are predictive of individual behavioral preferences. These circuit elements can be
366 considered loci of individuality, as they appear to harbor the origins of idiosyncratic preferences
367 among isogenic animals reared in the same environment. Specifically, the total responsiveness of
368 ORNs predicts idiosyncratic odor-vs-air preferences, and contrasting glomerular activation in
369 PNs predicts idiosyncratic odor-vs-odor preferences (Figures 1, 2). Both of these circuit elements
370 are in the olfactory sensory periphery, suggesting that behavioral idiosyncrasy arises early in the
371 sensorimotor transformation. We were particularly surprised at the extent to which PN activity
372 could predict preference between two aversive odors. We estimated that the strength of the
373 correlation between latent PN activity and behavioral states was 0.75 (Figure 4B).

374

375 Previous work has found mammalian peripheral circuit areas are predictive of individual
376 behavior (Britten et al., 1996; Michelson et al., 2017; Newsome et al., 1989; Osborne et al.,
377 2005), but this study is among the first (Linneweber et al., 2020; Mellert et al., 2016; Skutt-
378 Kakaria et al., 2019) to link cellular-level circuit variants and individual behavior in the absence
379 of genetic variation. Another key conclusion is that loci of individuality are likely to vary, even
380 within the sensory periphery, with the specific behavioral paradigm (i.e., odor-vs-odor or odor-
381 vs-air). Our ability to predict behavioral preferences was limited by the repeatability of the
382 behavior itself (Figure 4 – figure supplement 1). Low persistence of odor preference may be
383 attributable to factors like internal states or plasticity. It may be fruitful in future studies to map
384 circuit elements whose activity predicts trial-to-trial behavioral fluctuations within individuals.

385

386 Seeking insight into the molecular basis of behaviorally-relevant physiological variation, we
387 imaged Brp in the axon terminals of the ORN-PN synapse, using confocal and expansion
388 microscopy. Brp glomerular (and probably puncta) density was a predictor of individual odor-vs-
389 odor preferences (Figure 3). Higher Brp in DM2 predicted stronger MCH preference, like higher
390 calcium responses in DM2 PNs, suggesting that variation in PN inputs underlies PN
391 physiological variation. This is consistent with the recent finding of a linear relationship between
392 synaptic density and excitatory postsynaptic potentials (Liu et al., 2022) and another study in
393 which idiosyncratic synaptic density in central complex output neurons predicts individual
394 locomotor behavior (Skutt-Kakaria et al., 2019). The predictive relationship between Brp and
395 behavior was weaker than that of PN calcium responses, suggesting there are other determinants,

396 such as other synaptic proteins, neurite morphology, or the influence of idiosyncratic LNs (Chou
397 et al., 2010) modulating the ORN-PN transformation (Nagel et al., 2015).

398

399 To integrate our synaptic and physiological results, we implemented a spiking model with 3,062
400 neurons and synaptic weights drawn directly from the fly connectome (Scheffer et al., 2020)
401 (Figure 5). With light parameter tuning, this model recapitulated canonical AL computations,
402 providing a baseline for assessing the effects of idiosyncratic stochastic variation. The apparent
403 variation in odor responses across simulated individuals (Figure 5F) is less than that seen in the
404 empirical calcium responses (Figure 1H), likely due to 1) biological phenomena missing from
405 the model, 2) the lack of measurement noise, and 3) the fact that our perturbations are applied to
406 the connectome of a single fly. When examining PCA loadings, however, simulating
407 idiosyncratic ALs by varying PN input synapse density or bootstrapping ORNs produced
408 correlated PN responses across odors in DC2 and DM2, matching our experimental results.
409 These sources of variation specifically implicate the ORN-PN synapse (like our Brp results) as
410 an important substrate for establishing behaviorally-relevant patterns of PN response variation.

411

412 The flies used in our experiments were isogenic and reared in standardized laboratory conditions
413 that produce reduced behavioral individuality compared to enriched environments (Akhund-Zade
414 et al., 2019; Körholz et al., 2018; Zocher et al., 2020). Yet, even these conditions yield
415 substantial behavioral individuality. We do not expect variability in the expression of the flies'
416 transgenes to be a major driver of this individuality, as wildtype flies have a similarly broad
417 distribution of odor preferences (Honegger et al., 2019). The ultimate source of stochasticity in
418 this behavior remains a mystery, with possibilities ranging from thermal fluctuations at the
419 molecular scale to macroscopic, but seemingly irrelevant, variations like the exact fill level of the
420 culture media (Honegger and de Bivort, 2018). Developing nervous systems employ various
421 compensation mechanisms to dampen out the effects of these fluctuations (Marder, 2011; Tobin
422 et al., 2017). Behavioral variation may be beneficial, supporting a bet-hedging strategy (Hopper,
423 1999) to counter environmental fluctuations (Akhund-Zade et al., 2020; Honegger et al., 2019;
424 Kain et al., 2015; Krams et al., 2021). Empirically, the net effect of dampening and accreted
425 ontological (Gomez-Marin and Ghazanfar, 2019) fluctuations is individuals with diverse
426 behaviors. This process unfolds across all levels of biological regulation. Just as PN response
427 variation appears to be partially rooted in glomerular Brp variation, the latter has its own
428 molecular roots, including, perhaps, stochasticity in gene expression (Li et al., 2017; Raj et al.,
429 2010), itself a predictor of idiosyncratic behavioral biases (Werkhoven et al., 2021). Improved
430 methods to longitudinally assay the fine-scale molecular and anatomical makeup of behaving
431 organisms throughout development and adulthood will be invaluable to further illuminate the
432 mechanistic origins of individuality.

433

434 **Materials and Methods**

435

436 ***Data and code availability***

437 All raw data, totaling 600 GB, are available via hard drive from the authors. A smaller (7 GB)
438 repository with partially processed data files and MATLAB/Python scripts sufficient to generate
439 figures and results is available at Zenodo ([doi:10.5281/zenodo.8092972](https://doi.org/10.5281/zenodo.8092972)).

440

441 ***Fly rearing***

442 Experimental flies were reared in a *Drosophila* incubator (Percival Scientific DR-36VL) at 22°
443 C, 40% relative humidity, and 12:12h light:dark cycle. Flies were fed cornmeal/dextrose
444 medium, as previously described (Honegger et al., 2019). Mated female flies aged 3 days post-
445 eclosion were used for behavioral persistence experiments. Mated female flies aged 7 to 15 days
446 post-eclosion were used for all paired behavior-calcium imaging and immunohistochemistry
447 experiments.

448

449 ***Fly stocks***

450 The following stocks were obtained from the Bloomington *Drosophila* Stock Center:
451 P{20XUAS-IVS-GCaMP6m}attP40 (BDSC #42748), w[*]; P{w[+mC]=Or13a-GAL4.F}40.1
452 (BDSC #9945), w[*]; P{w[+mC]=Or19a-GAL4.F}61.1 (BDSC #9947), w[*];
453 P{w[+mC]=Or22a-GAL4.7.717}14.2 (BDSC #9951), w[*]; P{w[+mC]=Orco-GAL4.W}11.17;
454 TM2/TM6B, Tb[1] (BDSC #26818). Transgenic lines were outcrossed to the isogenic line
455 isokh11 (Honegger et al., 2019) for at least 5 generations prior to being used in any experiments.
456 GH146-Gal4 was a gift provided by Y. Zhong (Honegger et al., 2019). w; UAS-Brp-Short-
457 mStrawberry; UAS-mCD8-GFP; + was a gift of Timothy Mosca and was not outcrossed to the
458 isokh11 background (Mosca and Luo, 2014).

459

460 ***Odor delivery***

461 Odor delivery during behavioral tracking and neural activity imaging was controlled with
462 isolation valve solenoids (NResearch Inc.) (Honegger et al., 2019). Saturated headspace from 40
463 ml vials containing 5 ml pure odorant were serially diluted via carbon-filtered air to generate a
464 variably (10-25%) saturated airstream controlled by digital flow controllers (Alicat Scientific)
465 and presented to flies at total flow rates of ~100 mL/min. The odor panel used for imaging was
466 comprised of the following odorants: 2-heptanone (CAS #110-43-0, Millipore Sigma), 1-
467 pentanol (CAS #71-41-0, Millipore Sigma), 3-octanol (CAS #589-98-0, Millipore Sigma), hexyl-
468 acetate (CAS #142-92-7, Millipore Sigma), 4-methylcyclohexanol (CAS #589-91-3, Millipore
469 Sigma), pentyl acetate (CAS #628-63-7, Millipore Sigma), 1-butanol (CAS #71-36-3, Millipore
470 Sigma), ethyl lactate (CAS #97-64-3, Millipore Sigma), geranyl acetate (CAS #105-87-3,
471 Millipore Sigma), 1-hexanol (CAS #111-27-34, Millipore Sigma), citronella java essential oil (
472 191112, Aura Cacia), and 200 proof ethanol (V1001, Decon Labs).

473

474 ***Odor preference behavior***

475 Odor preference was measured at 25°C and 20% relative humidity. As previously described
476 (Honegger et al., 2019), individual flies confined to custom-fabricated tunnels were illuminated
477 with infrared light and behavior was recorded with a digital camera (Basler) and zoom lens
478 (Pentax). The odor choice tunnels were 50 mm long, 5 mm wide, and 1.3 mm tall. Custom real-
479 time tracking software written in MATLAB was used to track centroid, velocity, and principal
480 body axis angle throughout the behavioral experiment, as previously described (Honegger et al.,
481 2019). After a 3-minute acclimation period, odorants were delivered to either end of the tunnel
482 array for 3 minutes. Odor preference score was calculated as the fraction of time spent in the
483 reference side of the tunnel during odor-on period minus the time spent in the reference side of
484 the tunnel during the pre-odor acclimation period.

485

486 ***Behavioral preference persistence measurements***

487 After measuring odor preference, flies were stored in individual housing fly plates (modified 96-
488 well plates; FlySorter, LLC) on standard food, temperature, humidity, and lighting conditions.
489 Odor preference of the same individuals was measured 3 and/or 24 hours later. In some cases, fly
490 tunnel position was randomized between measurements. We observed that randomization had
491 little effect on preference persistence.

492

493 ***Calcium imaging***

494 Flies expressing GCaMP6m in defined neural subpopulations were imaged using a custom-built
495 two-photon microscope and ultrafast Ti:Sapphire laser (Spectra-Physics Mai Tai) tuned to 930
496 nm, at a power of 20 mW out of the objective (Olympus XLUMPlanFL N 20x/1.00 W). For
497 paired behavior and imaging experiments, the time elapsed between behavior measurement and
498 imaging ranged from 15 minutes to 3 hours. Flies were anesthetized on ice and immobilized in
499 an aluminum sheet with a female-fly-sized hole cut in it. The head cuticle between the antennae
500 and ocelli was removed along with the tracheae to expose the ALs from the dorsal side. Volume
501 scanning was performed using a piezoelectric objective mount (Physik Instrumente). ScanImage
502 2013 software (Vidrio Technologies) was used to coordinate galvanometer laser scanning and
503 image acquisition. Custom Matlab (Mathworks) scripts were used to coordinate image
504 acquisition and control odor delivery. 256 by 192 (x-y) pixel 16-bit tiff images were recorded.
505 The piezo travel distance was adjusted between 70 and 90 μm so as to cover most of the AL. The
506 number of z-sections in a given odor panel delivery varied between 7 and 12 yielding a volume
507 acquisition rate of 0.833 Hz. Odor delivery occurred from 6-9.6s of each recording.

508

509 Each fly experienced up to four deliveries of the odor panel. The antennal lobe being recorded
510 (left or right) was alternated after each successful completion of an odor panel. Odors were
511 delivered in randomized order. In cases where baseline fluorescence was very weak or no
512 obvious odor responses were visible, not all four panels were delivered.

513

514 ***Glomerulus segmentation and labeling***

515 Glomerular segmentation masks were extracted from raw image stacks using a *k*-means
516 clustering algorithm based on time-varying voxel fluorescence intensities, as previously
517 described (Honegger et al., 2019). Each image stack, corresponding to a single odor panel
518 delivery, was processed individually. Time-varying voxel fluorescence values for each odor
519 delivery were concatenated to yield a voxel-by-time matrix consisting of each voxel's recorded
520 value during the course of all 13 odor deliveries of the odor panel. After z-scoring, principal
521 component analysis was performed on this matrix and 75% of the variance was retained. Next, *k*-
522 means (*k*=80, 50 replicates with random starting seeds) was performed to produce 50 distinct
523 voxel cluster assignment maps which we next used to calculate a consensus map. This approach
524 was more accurate than clustering based on a single *k*-means seed.

525
526 Of the 50 generated voxel cluster assignment maps, the top 5 were selected by choosing those
527 maps with the lowest average within-cluster sum of distances, selecting for compact glomeruli.
528 The remaining maps were discarded. Next, all isolated voxel islands in each of the top 5 maps
529 were identified and pruned based on size (minimum size = 100 voxels, maximum size = 10000
530 voxels). Finally, consensus clusters were calculated by finding voxel islands with significant
531 overlap across all 5 of the pruned maps. Voxels which fell within a given cluster across all 5
532 pruned maps were added to the consensus cluster. This process was repeated for all clusters until
533 the single consensus cluster map was complete. In some cases we found by manual inspection
534 that some individual glomeruli were clearly split into two discrete clusters. These splits were
535 remedied by automatically merging all consensus clusters whose centroids were separated by a
536 physical distance of less than 30 voxels and whose peak odor response Spearman correlation was
537 greater than 0.8. Finally, glomeruli were manually labeled based on anatomical position,
538 morphology, and size (Grabe et al., 2015). We focused our analysis on 5 glomeruli (DM1, DM2,
539 DM3, DL5, and DC2), which were the only glomeruli that could be observed in all paired
540 behavior-calcium datasets. However, not all 5 glomeruli were identified in all recordings (Figure
541 1 – figure supplement 3). Missing glomerular data was later mean-imputed.

542
543 ***Calcium image data analysis***

544 All data was processed and analyzed in MATLAB 2018a (Mathworks). Calcium responses for
545 each voxel were calculated as $\Delta f/f = [f(t) - F]/F$, where *f*(*t*) and *F* are the instantaneous and
546 average fluorescence, respectively. Each glomerulus' time-dependent calcium response was
547 calculated as the mean $\Delta f/f$ across all voxels falling within the glomerulus' automatically-
548 generated segmentation mask during a single volume acquisition. Time-varying odor responses
549 were normalized to baseline by subtracting the median of pre-odor $\Delta f/f$ from each trace. Peak
550 odor response was calculated as the maximum fluorescence signal from 7.2s to 10.8s (images 6
551 through 9) of the recording.

552

553 To compute principal components of calcium dynamics, each fly's complement of odor panel
554 responses (a 5 glomeruli by 13 odors = 65-dimensional vector) was concatenated. Missing
555 glomerulus-odor response values were filled in with the mean glomerulus-odor pair across all fly
556 recordings for which the data was not missing. After infilling, principal component analysis was
557 carried out with individual odor panel deliveries as observations and glomerulus-odor responses
558 pairs as features.

559
560 Inter- and intra-fly distances (Figure 1J) were calculated using the projections of each fly's
561 glomerulus-odor responses onto all principal components. For each fly, the average Euclidean
562 distance between response projections 1) among left lobe trials, 2) among right lobe trials, and 3)
563 between left and right lobe trials were averaged together to get a single within-fly distance. Intra-
564 fly distances were computed in a similar fashion (for each fly, taking the average distance of its
565 response projections to those of other flies using only left lobe trials / only right lobe trials /
566 between left-right trials, then averaging these three values to get a single across-fly distance).

567
568 In a subset of experiments in which we imaged calcium activity, some solenoids failed to open,
569 resulting in the failure of odor delivery in a small number of trials. In these cases, we identified
570 trials with valve failures by manually recognizing that glomeruli failed to respond during the
571 nominal odor period. These trials were treated as missing data and infilled, as described above.
572 Fewer than ~10% of flies and 5% of odor trials were affected.

573
574 For all predictive models constructed, the average principal component score or glomerulus-odor
575 $\Delta f/f$ response across trials was used per individual; that is, each fly contributed one data point to
576 the relevant model. Linear models were constructed from behavior scores and the relevant
577 predictor (principal component, average $\Delta f/f$ across dimensions, specific glomerulus
578 measurements) as described in the text and Tables 1-2. 95% confidence intervals around model
579 regression lines were estimated as ± 2 standard deviations of the value of the regression line at
580 each x-position across 2000 bootstrap replicates (resampling flies). To predict behavior as a
581 function of time during odor delivery, we analyzed data as described above, but considered only
582 $\Delta f/f$ at each single time point (Figure 4 – figure supplement 2A-C), rather than averaging during
583 the peak response interval.

584
585 To decode individual identity from neural responses, we first performed PCA on individual odor
586 panel peak responses. We retained principal component scores constituting specified fractions of
587 variance (Figure 1 – figure supplement 5A) and trained a linear logistic classifier to predict
588 individual identity from single odor panel deliveries.

589
590 To decode odor identity from neural responses, each of the 5 recorded glomeruli were used as
591 features, and the calcium response of each glomerulus to a specific odor at a specified time point
592 were used as observations (PNs, n=5317 odor deliveries; ORNs, n=2704 odor deliveries). A

593 linear logistic classifier was trained to predict the known odor identity using 2-fold cross-
594 validation. That is, a model was trained on half the data and evaluated on the remaining half, and
595 then this process was repeated with the train and test half reversed. The decoding accuracy was
596 quantified as the fraction of odor deliveries in which the predicted odor was correct.

597

598 ***Inference of correlation between latent calcium and behavior states***

599 We performed a simulation-based analysis to infer the strength of the correlation between latent
600 calcium (Brp) and behavior states, given the R^2 of a given linear model. Figure 4 – figure
601 supplement 1A is a schematic of the data generation process we assume underlies our observed
602 data. We assume that the “true” behavioral and calcium values of the animal are captured by
603 unobserved latent states X_c and X_b , respectively, such that the correlation between X_c and X_b is the
604 biological signal captured by the model, having adjusted for the noise associated with actually
605 measuring behavior and calcium (ρ_{signal}). Our calcium and odor preference scores are subject to
606 measurement error and temporal instability (behavior and neural activity were measured 1-3
607 hours apart). These effects are both noise with respect to estimating the linear relationship
608 between calcium and behavior. Their magnitude can be estimated using the empirical
609 repeatability of behavior and calcium experiments respectively. Thus, our overall approach was
610 to assume true latent behavior and calcium signals that are correlated at the level ρ_{signal} , add noise
611 to them commensurate with the repeatability of these measures to simulate measured behavior
612 and calcium, and record the simulated empirical R^2 between these measured signals. This was
613 done many times to estimate distributions of empirical R^2 given ρ_{signal} . These distributions could
614 finally be used in the inverse direction to infer ρ_{signal} given the actual model R^2 values computed
615 in our study.

616

617 Specifically, we simulated X_c as a set of N standard normal variables (N equalling the number of
618 flies used to compute a correlation between predicted and measured preference) and generated X_b
619 $= \rho_{signal} X_c + (1 - \rho_{signal}^2 Z)^{1/2}$, where Z is a set of N standard normal variables uncorrelated with X_c , a
620 procedure that ensures that $corr(X_c, X_b) = \rho_{signal}$. Next, we simulated observed calcium readouts
621 X_c' and X_c'' , such that $corr(X_c, X_c') = corr(X_c, X_c'') = r_c$. Similarly, we simulated noisy observed
622 behavioral assay readouts X_b' and X_b'' , such that $corr(X_b, X_b') = corr(X_b, X_b'') = r_b$. The values
623 of r_c and r_b were fixed by the empirical repeatability of calcium (R_{c,c^2}) and behavior (R_{b,b^2})
624 respectively as follows. Since calcium is a multidimensional measure, and our calcium model
625 predictors are based on principal components of glomerulus-odor responses, we used variance
626 explained along the PCs to calculate a single value for the calcium repeatability R_{c,c^2} . We
627 compared the eigenvalues of the real calcium PCA to those of shuffled calcium data (shuffling
628 glomerulus/odor responses for each individual fly), computing R_{c,c^2} by summing the variance
629 explained along the PCs of the calcium data up until the component-wise variance for the
630 calcium data fell below that of the shuffled data, a similar approach as done in Berman et al.,
631 2014 and Werkhoven et al., 2021. R_{c,c^2} was calculated to be 0.77 for both ORN and PN calcium;
632 we set $r_c = (R_{c,c^2})^{1/4}$ to ensure $corr(X_c', X_c'')^2 = R_{c,c^2}$. We matched r_b to the repeatability across

633 odor preference trials in the same flies measured 3h apart ($R_{b,b^2}=0.23$ for OCT vs AIR, and 0.12
634 for OCT vs MCH, Figure 1 – figure supplement 1B-D), setting $r_b = (R_{b,b^2})^{1/4}$ to ensure $\text{corr}(X_b',$
635 $X_b'')^2 = R_{b,b^2}$.

636
637 We varied ρ_{signal} from 0 to 1 in increments of 0.01, and for each ρ_{signal} , we simulated a set of N X_c
638 and generated $X_b, X_c', X_c'', X_b',$ and X_b'' , then we computed a simulated observed calcium-
639 behavior relationship strength $R_{c,b^2} = \text{corr}(X_c', X_b')^2$. We repeated this simulation 10,000 times
640 for each ρ_{signal} and plotted the resultant relationship between ρ_{signal} against R_{c,b^2} (percentiles of
641 R_{c,b^2} are displayed in Figure 4 – figure supplement 1B). Then, for each linear model of interest,
642 we inferred ρ_{signal} by extracting the marginal distribution of ρ_{signal} near the model's R^2 (+/- 20%)
643 and report the median ρ_{signal} .

644
645 The procedure outlined above was done analogously for models using Brp-short relative
646 fluorescence intensity, performing the PCA-based calcium response repeatability step with PCA
647 on the multidimensional Brp-short relative fluorescence intensity (which yielded $R_{brp,brp^2} =$
648 0.75).

649 **DoOR data**

651 DoOR data for the glomeruli and odors relevant to our study was downloaded from
652 <http://neuro.uni-konstanz.de/DoOR/default.html> (Münch and Galizia, 2016).

653 **Yoked odor experience experiments**

655 We selected six flies for which both odor preference and neural activity were recorded to serve
656 as the basis for imposed odor experiences for yoked control flies. The experimental flies were
657 chosen to represent a diversity of preference scores. Each experimental fly's odor experience was
658 binned into discrete odor bouts to represent experience of either MCH or OCT based on its
659 location in the tunnel as a function of time (Figure 2J). Odor bouts lasting less than 100 ms were
660 omitted due to limitations on odor-switching capabilities of the odor delivery apparatus. To
661 deliver a given experimental fly's odor experience to yoked controls, we set both odor streams
662 (on either end of the tunnel apparatus) to deliver the same odor experienced by the experimental
663 fly at that moment during the odor-on period. No odor was delivered to yoked controls during
664 time points in which the experimental fly resided in the tunnel choice zone (central 5 mm). See
665 Figure 2J for an example pair of experimental fly and yoked control behavior and odor
666 experience.

667 **Immunohistochemistry**

669 After measuring odor preference behavior, 7-15 day-old flies were anesthetized on ice and brains
670 were dissected in phosphate buffered saline (PBS). Dissection and immunohistochemistry were
671 carried out as previously reported (Wu and Luo, 2006). The experimenter was blind to the
672 behavioral scores of all individuals throughout dissection, imaging, and analysis. Individual

673 identities were maintained by fixing, washing, and staining each brain in an individual 0.2 mL
674 PCR tube using fluid volumes of 100 μ L per brain (Fisher Scientific). Primary incubation
675 solution contained mouse anti-nc82 (1:40, DSHB), chicken anti-GFP (1:1000, Aves Labs), rabbit
676 anti-mStrawberry (1:1000, biorbyt), and 5% normal goat serum (NGS, Invitrogen) in PBT (0.5%
677 Triton X-100 in PBS). Secondary incubation solution contained Atto 647N-conjugated goat anti-
678 mouse (1:250, Millipore Sigma), Alexa Fluor 568-conjugated goat anti-rabbit (1:250), Alexa
679 Fluor 488-conjugated goat anti-chicken (1:250, ThermoFisher), and 5% NGS in PBT. Primary
680 and secondary incubation times were 2 and 3 overnights, respectively, at 4° C. Stained samples
681 were mounted and cleared in Vectashield (H-1000, Vector Laboratories) between two coverslips
682 (12-568B, Fisher Scientific). Two reinforcement labels (5720, Avery) were stacked to create a
683 0.15 mm spacer.

684

685 ***Expansion microscopy***

686 Immunohistochemistry for expansion microscopy was carried out as described above, with the
687 exception that antibody concentrations were modified as follows: mouse anti-nc82 (1:40),
688 chicken anti-GFP (1:200), rabbit anti-mStrawberry (1:200), Atto 647N-conjugated goat anti-
689 mouse (1:100), Alexa Fluor 568-conjugated goat anti-rabbit (1:100), Alexa Fluor 488-conjugated
690 goat anti-chicken (1:100). Expansion of stained samples was performed as previously described
691 (Asano et al., 2018; Gao et al., 2019). Expanded samples were mounted in coverslip-bottom petri
692 dishes (MatTek Corporation) and anchored by treating the coverslip with poly-l-lysine solution
693 (Millipore Sigma) as previously described (Asano et al., 2018).

694

695 ***Confocal imaging***

696 All confocal imaging was carried out at the Harvard Center for Biological Imaging. Unexpanded
697 samples were imaged on an LSM700 (Zeiss) inverted confocal microscope equipped with a 40x
698 oil-immersion objective (1.3 NA, EC Plan Neofluar, Zeiss). Expanded samples were imaged on
699 an LSM880 (Zeiss) inverted confocal microscope equipped with a 40x water-immersion
700 objective (1.1 NA, LD C-Apochromat, Zeiss). Acquisition of Z-stacks was automated with Zen
701 Black software (Zeiss).

702

703 ***Standard confocal image analysis***

704 We used custom semi-automated code to generate glomerular segmentation masks from confocal
705 z-stacks of unexpanded Orco>Brp-Short brains. Using Matlab, each image channel was median
706 filtered ($\sigma_x, \sigma_y, \sigma_z = 11, 11, 1$ pixels) and downsampled in x and y by a factor of 11. Next, an
707 ORN mask was generated by multiplying and thresholding the Orco>mCD8 and Orco>Brp-Short
708 channels. Next, a locally normalized nc82 and Orco>mCD8 image stack were multiplied and
709 thresholded, and the ORN mask was applied to remove background and other undesired brain
710 structures. This pipeline resulted in a binary image stack which maximized the contrast of the
711 glomerular structure of the antennal lobe. We then applied a binary distance transform and

712 watershed transform to generate discrete subregions which aimed to represent segmentation
713 masks for each glomerulus tagged by Orco-Gal4.

714

715 However, this procedure generally resulted in some degree of under-segmentation; that is, some
716 glomerular segmentation masks were merged. To split each merged segmentation mask, we
717 convolved a ball (whose radius was proportional to the cube root of the volume of the
718 segmentation mask in question) across the mask and thresholded the resulting image. The
719 rationale of this procedure was that 2 merged glomeruli would exhibit a mask shape resembling
720 two touching spheres, and convolving a similarly-sized sphere across this volume followed by
721 thresholding would split the merged object. After ball convolution, we repeated the distance and
722 watershed transform to once more generate discrete subregions representing glomerular
723 segmentation masks. This second watershed step generally resulted in over-segmentation; that is,
724 by visual inspection it was apparent that many glomeruli were split into multiple subregions.
725 Therefore, we finally manually agglomerated the over-segmented subregions to generate single
726 segmentation masks for each glomerulus of interest. We used a published atlas to aid manual
727 identification of glomeruli (Grabe et al., 2015). The total Brp-Short fluorescence signal within
728 each glomerulus was determined and divided by the volume of the glomerulus' segmentation
729 mask to calculate Brp-Short density values.

730

731 *Expansion microscopy image analysis*

732 The spots function in Imaris 9.0 (Bitplane) was used to identify individual Brp-Short puncta in
733 expanded sample image stacks of Or13a>Brp-Short samples (Mosca and Luo, 2014). The spot
734 size was set to 0.5 μm , background subtraction and region-growing were enabled, and the default
735 spot quality threshold was used for each image stack. Identified spots were used to mask the Brp-
736 Short channel and the resultant image was saved as a new stack. In MATLAB, a glomerular
737 mask was generated by smoothing ($\sigma_x, \sigma_y, \sigma_z = 40, 40, 8$ pixels) and thresholding (92.5th
738 percentile) the raw Brp-Short image stack. The mask was then applied to the spot image stack to
739 remove background spots. Finally, the masked spot image stack was binarized and spot number
740 and properties were quantified.

741

742 *Antennal Lobe modeling*

743 We constructed a model of the antennal lobe to test the effect of circuit variation on PN activity
744 variation across individuals. Our general approach to producing realistic circuit activity with the
745 AL model was 1) using experimentally-measured parameters whenever possible (principally the
746 connectome wiring diagram and biophysical parameters measured electrophysiologically), 2)
747 associating free parameters only with biologically plausible categories of elements, while
748 minimizing their number, and 3) tuning the model using those free parameters so that it
749 reproduced high-level patterns of activity considered in the field to represent the canonical
750 operations of the AL. Simulations were run in Python (version 3.6) (van Rossum and Drake,
751 2011), and model outputs were analyzed using Jupyter notebooks (Kluyver et al., 2016) and

752 Python and Matlab scripts.

753

754 ***AL model neurons***

755 Release 1.2 of the hemibrain connectomics dataset (Scheffer et al., 2020) was used to set the
756 connections in the model. Hemibrain body IDs for ORNs, LNs, and PNs were obtained via the
757 lists of neurons supplied in the supplementary tables in Schlegel et al., 2020. ORNs and PNs of
758 non-olfactory glomeruli (VP1d, VP1l, VP1m, VP2, VP3, VP4, VP5) were ignored, leaving 51
759 glomeruli. Synaptic connections between the remaining 2574 ORNs, 197 LNs, 166 mPNs, and
760 130 uPNs were queried from the hemibrain API. All ORNs were assigned to be excitatory
761 (Wilson, 2013). Polarities were assigned to PNs based on the neurotransmitter assignments in
762 Bates et al., 2020. mPNs without neurotransmitter information were randomly assigned an
763 excitatory polarity with probability equal to the fraction of neurotransmitter-identified mPNs that
764 are cholinergic; the same process was performed for uPNs. After confirming that the model's
765 output was qualitatively robust to which mPNs and uPNs were randomly chosen, this random
766 assignment was performed once and then frozen for subsequent analyses.

767

768 Of the 197 LNs, we assigned 31 to be excitatory, based on the estimated 1:5.4 ratio of eLNs to
769 iLNs in the AL (Tsai et al., 2018). To account for observations that eLNs broadly innervate the
770 AL (Shang et al., 2007), all LNs were ranked by the number of innervated glomeruli, and the 31
771 eLNs were chosen uniformly at random from the top 50% of LNs in the list. This produced a
772 distribution of glomerular innervations in eLNs qualitatively similar to that of *krasavietz* LNs in
773 Supplementary Figure 6 of Chou et al., 2010.

774

775 ***Voltage model***

776 We used a single-compartment leaky-integrate-and-fire voltage model for all neurons as in
777 Kakaria and de Bivort, 2017, in which each neuron had a voltage $V_i(t)$ and current $I_i(t)$. When the
778 voltage of neuron i was beneath its threshold $V_{i,thr}$, the following dynamics were obeyed:

779

$$780 \quad C_i \frac{dV_i}{dt} = \frac{V_{i,0} - V_i(t)}{R_i} + I_{i,odor}(t) + \sum_{j=1}^N a_j W_{ji} I_j(t)$$

781

782 Each neuron i had electrical properties: membrane capacitance C_i , resistance R_i , and resting
783 membrane potential $V_{i,0}$ with values from electrophysiology measurements (Table 2).

784

785 When the voltage of a neuron exceeded the threshold $V_{i,thr}$, a templated action potential was
786 filled into its voltage time trace, and a templated postsynaptic current was added to all
787 downstream neurons, following the definitions in Kakaria and de Bivort, 2017.

788

789 Odor stimuli were simulated by triggering ORNs to spike at frequencies matching known
790 olfactory receptor responses to the desired odor. The timing of odor-evoked spikes was given by

791 a Poisson process, with firing rate FR for ORNs of a given glomerulus governed by:

792

$$793 \quad FR_{glom,odor}(t) = FR_{max} D_{glom,odor} (f_a + (1 - f_a) e^{-t/t_a})$$

794

795 FR_{max} , the maximum ORN firing rate, was set to 400 Hz. $D_{glom,odor}$ is a value between 0 and 1
796 from the DoOR database, representing the response of an odorant receptor/glomerulus to an
797 odor, estimated from electrophysiology and/or fluorescence data (Münch and Galizia, 2016).

798 ORNs display adaptation to odor stimuli (Wilson, 2013), captured by the final term with

799 timescale $t_a = 110 \text{ ms}$ to 75% of the initial value, as done in Kao and Lo, 2020. Thus, the

800 functional maximum firing rate of an ORN was 75% of 400 Hz = 300 Hz, matching the highest

801 ORN firing rates observed experimentally (Hallem et al., 2004). After determining the times of

802 ORN spikes according to this firing-rate rule, spikes were induced by the addition of 10^6

803 picoamps in a single time step. This reliably triggered an action potential in the ORN, regardless

804 of currents from other neurons. In the absence of odors, spike times for ORNs were drawn by a

805 Poisson process at 10 Hz, to match reported spontaneous firing rates (de Bruyne et al., 2001).

806

807 For odor-glomeruli combinations with missing DoOR values (40% of the dataset), we performed

808 imputation via alternating least squares (using the `pca` function with option ‘als’ to infill missing

809 values ([MATLAB documentation](#)) on the odor x glomerulus matrix 1000 times and taking the

810 mean infilled matrix, which provides a closer match to ground truth missing values than a single

811 run of ALS (Figure 1 – figure supplement 5 of Werkhoven et al., 2021).

812

813 A neuron j presynaptic to i supplies its current $I_j(t)$ scaled by the synapse strength W_{ji} , the

814 number of synapses in the hemibrain dataset from neuron j to i . Rows in W corresponding to

815 neurons with inhibitory polarity (i.e. GABAergic PNs or LNs) were set negative. Finally, post-

816 synaptic neurons (columns of the connectivity matrix) have a class-specific multiplier a_i , a hand-

817 tuned value, described below.

818

819 ***AL model tuning***

820 Class-specific multiplier current multipliers (a_i) were tuned using the panel of 18 odors from

821 Bhandawat et al., 2007 (our source for several experimental observations of high-level AL

822 function): benzaldehyde, butyric acid, 2,3-butanedione, 1-butanol, cyclohexanone, Z3-hexenol,

823 ethyl butyrate, ethyl acetate, geranyl acetate, isopentyl acetate, isoamyl acetate, 4-methylphenol,

824 methyl salicylate, 3-methylthio-1-propanol, octanal, 2-octanone, pentyl acetate, E2-hexenal,

825 trans-2-hexenal, gamma-valerolactone. Odors were “administered” for 400 ms each, with 300 ms

826 odor-free pauses between odor stimuli.

827

828 The high-level functions of the AL that represent a baseline, working condition were: (1) firing

829 rates for ORNs, LNs, and PNs matching the literature (listed in Table 2 and see (Bhandawat et

830 al., 2007; Dubin and Harris, 1997; Jeanne and Wilson, 2015; Seki et al., 2010), (2) a more

831 uniform distribution of PN firing rates during odor stimuli compared to ORN firing rates, (3)
832 greater separation of representations of odors in PN-coding space than in ORN-coding space, and
833 (4) a sublinear transfer function between ORN firing rates and PN firing rates. Features (2) - (4)
834 relate to the role of the AL in enhancing the separability of similar odors (Bhandawat et al.,
835 2007).

836
837 To find a parameterization with those functions, we tuned the values of a_i as scalar multipliers on
838 ORN, eLN, iLN, and PN columns of the hemibrain connectivity matrix. Thus, these values
839 represent cell type-specific sensitivities to presynaptic currents, which may be justified by the
840 fact that ORNs/LNs/PNs are genetically distinct cell populations (McLaughlin et al., 2021; Xie
841 et al., 2021). A grid search of the four class-wise sensitivity parameters produced a configuration
842 that reasonably satisfied the above criteria (Figure 5 – figure supplement 2). In this
843 configuration, the ORN columns of the hemibrain connectivity matrix are scaled by 0.1, eLNs by
844 0.04, iLNs by 0.02, and PNs by 0.4. The relatively large multiplier on PNs is potentially
845 consistent with the fact that PNs are sensitive to small differences between weak ORN inputs
846 (Bhandawat et al., 2007). Model outputs were robust over several different sets of a_i , provided
847 iLN sensitivity \approx eLN < ORN < PN.

848
849 We analyzed the sensitivity of the model's parameters around their baseline values of a_{ORN} , a_{eLN} ,
850 a_{iLN} , $a_{PN} = (0.1, 0.04, 0.02, 0.4)$. Each parameter was independently scaled up to 4x or 1/4x of its
851 baseline value (Figure 5 – figure supplement 3), and the PN firing rates recorded. Separately,
852 multiple-parameter manipulations were performed by multiplying each parameter by a random
853 log-Normal value with mean 1 and +/-1 standard deviation corresponding to a 2x or 0.5x scaling
854 on each parameter. Mean PN-odor responses were calculated for all manipulated runs and
855 compared to the mean PN-odor responses for the baseline configuration. A manipulation effect
856 size was calculated by cohen's d ((mean manipulated response - mean baseline response)/(pooled
857 standard deviation)). None of these manipulations reached effect size magnitudes larger than 0.9
858 (which can be roughly interpreted as the number of standard deviations in the baseline PN
859 responses away from the mean baseline PN response), which signaled that the model was robust
860 to the sensitivity parameters in this range. The most sensitive parameter was, unsurprisingly, a_{PN} .

861
862 Notable ways in which the model behavior deviates from experimental recordings (and thus
863 caveats on the interpretation of the model) include: 1) Model LNs appear to have more
864 heterogeneous firing rates than real LNs, with many LNs inactive for this panel of odor stimuli.
865 This likely reflects a lack of plastic/homeostatic mechanisms in the model to regularize LN firing
866 rates given their variable synaptic connectivity (Chou et al., 2010). 2) Some PNs had off-odor
867 rates that are high compared to real PNs, resulting in a distribution of ON-OFF responses that
868 had a lower limit than in real recordings. Qualitatively close matches were achieved between the
869 model and experimental data in the distributions of odor representations in ORN vs PN spaces
870 and the non-linearity of the ORN-PN transfer function.

871

872 ***AL model circuit variation generation***

873 We generated AL circuit variability in two ways: cell-type bootstrapping, and synapse density
874 resampling. These methods assume that the distribution of circuit configurations across
875 individual ALs can be generated by resampling circuit components within a single individual's
876 AL (neurons and glomerular synaptic densities, respectively, from the hemibrain EM volume).

877

878 To test the effect of variation in the developmental complement of neurons of particular types,
879 we bootstrapped populations of interest from the list of hemibrain neurons. Resampling with
880 replacement of ORNs was performed glomerulus-by-glomerulus, i.e., separately among each
881 pool of ORNs expressing a particular *Odorant receptor* gene. The same was done for PNs. For
882 LNs, all 197 LNs were treated as a single pool; there was no finer operation based on LN
883 subtypes or glomerular innervations. This choice reflects the high developmental variability of
884 LNs (Chou et al., 2010). The number of synapses between a pair of bootstrapped neurons was
885 equal to the synapse count between those neurons in the hemibrain connectivity matrix.

886

887 In some glomeruli, bootstrapping PNs produced unreasonably high variance in the total PN
888 synapse count. For instance, DP1m, DC4, and DM3 each harbor PNs that differ in total synapse
889 count by a factor of ~10. Since these glomeruli have between two to three PNs each, in a sizable
890 proportion of bootstrap samples, all-highly connected (or all-lowly) connected PNs are chosen in
891 such glomeruli. To remedy this biologically unrealistic outcome, we examined the relationship
892 between total input PN synapses within a glomerulus and glomerular volume (Figure 5 – figure
893 supplement 4). In the “synapse density resampling” method, we required that the number of PN
894 input synapses within a glomerulus reflect a draw from the empirical relationship between total
895 input PN synapses and glomerular volume as present in the hemibrain data set. This was
896 achieved by, for each glomerulus, sampling from the following distribution that depends on
897 glomerular volume, then multiplying the number of PN input synapses by a scalar to match that
898 sampled value:

899

$$900 \quad \log S_g = \log (a V_g^d) + \varepsilon_g, \varepsilon_g \sim N(0, \sigma^2)$$

901

902 Here S_g is the PN input synapse count for glomerulus g , V_g is the volume of glomerulus g (in
903 cubic microns), ε is a Gaussian noise variable with standard deviation σ , and a , d are the scaling
904 factor and exponent of the volume term, respectively. The values of these parameters ($a = 8.98$,
905 $d = 0.73$, $\sigma = 0.38$) were fit using maximum likelihood.

906

907 **Quantification and statistical analysis**

908 All fly behavior and calcium data was processed and analyzed in MATLAB 2018a (Mathworks).
909 AL simulations were run in Python (version 3.6) (van Rossum and Drake, 2011), and model
910 outputs were analyzed using Jupyter notebooks (Kluyver et al., 2016) and Python scripts. We

911 performed a power analysis prior to the study to determine that recording calcium activity in 20-
912 40 flies would be sufficient to identify moderate calcium-behavior correlations. Sample sizes for
913 expansion microscopy were smaller, as the experimental procedure was more involved –
914 therefore, we did not conduct a formal statistical analysis. Linear models were fit using the fitlm
915 MATLAB function (<https://www.mathworks.com/help/stats/fitlm.html>); coefficients and p-
916 values of models between measured preferences and predicted preferences are listed in Table 1.
917 95% confidence intervals around model regression lines were estimated as +/- 2 standard
918 deviations of the value of the regression line at each x-position across 2000 bootstrap replicates
919 (resampling flies). Boxplots depict the median value (points), interquartile range (boxes), and
920 range of the data (whiskers).

921

922 **Acknowledgments**

923 We thank Asa Barth-Marion and Rachel Wilson for discussions helpful to the AL modeling, and
924 Katrin Vogt for help revising the manuscript. Ed Soucy and Brett Graham of the Center for Brain
925 Science Neuroengineering Core helped maintain the olfactometer and microscope. D.L. was
926 supported by the NSF-Simons Center for Mathematical and Statistical Analysis of Biology at
927 Harvard, award number #1764269 and the Harvard Quantitative Biology Initiative. B.L.d.B. was
928 supported by a Klingenstein-Simons Fellowship Award, a Smith Family Odyssey Award, a
929 Harvard/MIT Basic Neuroscience Grant, National Science Foundation grant no. IOS-1557913,
930 and NIH/NINDS grant no. 1R01NS121874-01. E.B. was supported by a Harvard/MIT Basic
931 Neuroscience Grant, Lisa Yang, John Doerr, and NIH grant no. 1R01EB024261.

932

933 **Author contributions**

934 M.C. conducted behavior experiments with assistance from M.S., conducted confocal
935 microscopy, and conducted expansion microscopy with contributions from R. G. and E.B. D.L.
936 implemented the computational AL model. B.L.d.B. supervised the project.

937

938 **Declaration of interests**

939 E.B. is a co-founder of a company that aims to commercialize expansion microscopy for medical
940 purposes. R.G. and E.B. are co-inventors on multiple patents related to expansion microscopy.
941 The authors declare no other competing interests.

942 **References**

- 943 Akhund-Zade J, Ho S, O’Leary C, de Bivort B. 2019. The effect of environmental enrichment on
944 behavioral variability depends on genotype, behavior, and type of enrichment. *J Exp Biol*
945 **222**. doi:10.1242/jeb.202234
- 946 Akhund-Zade J, Yoon D, Bangerter A, Polizos N, Campbell M, Soloshenko A, Zhang T, Wice
947 E, Albright A, Narayanan A, Schmidt P, Saltz J, Ayroles J, Klein M, Bergland A, de Bivort
948 B. 2020. Wild flies hedge their thermal preference bets in response to seasonal fluctuations.
949 *bioRxiv*. doi:10.1101/2020.09.16.300731
- 950 Asano SM, Gao R, Wassie AT, Tillberg PW, Chen F, Boyden ES. 2018. Expansion Microscopy:
951 Protocols for Imaging Proteins and RNA in Cells and Tissues. *Curr Protoc Cell Biol*
952 **80**:e56. doi:10.1002/cpcb.56
- 953 Ayroles JF, Buchanan SM, O’Leary C, Skutt-Kakaria K, Grenier JK, Clark AG, Hartl DL, De
954 Bivort BL. 2015. Behavioral idiosyncrasy reveals genetic control of phenotypic variability.
955 *Proceedings of the National Academy of Sciences* **112**:6706–6711.
- 956 Bates AS, Schlegel P, Roberts RJV, Drummond N, Tamimi IFM, Turnbull R, Zhao X, Marin
957 EC, Popovici PD, Dhawan S, Jamasb A, Javier A, Serratos Capdevila L, Li F, Rubin GM,
958 Waddell S, Bock DD, Costa M, Jefferis GSXE. 2020. Complete Connectomic
959 Reconstruction of Olfactory Projection Neurons in the Fly Brain. *Curr Biol*.
960 doi:10.1016/j.cub.2020.06.042
- 961 Berman GJ, Choi DM, Bialek W, Shaevitz JW. 2014. Mapping the stereotyped behaviour of
962 freely moving fruit flies. *J R Soc Interface* **11**. doi:10.1098/rsif.2014.0672
- 963 Bhandawat V, Olsen SR, Gouwens NW, Schlieff ML, Wilson RI. 2007. Sensory processing in the
964 *Drosophila* antennal lobe increases reliability and separability of ensemble odor
965 representations. *Nat Neurosci* **10**:1474–1482. doi:10.1038/nn1976
- 966 Britten KH, Newsome WT, Shadlen MN, Celebrini S, Movshon JA. 1996. A relationship
967 between behavioral choice and the visual responses of neurons in macaque MT. *Vis*
968 *Neurosci* **13**:87–100. doi:10.1017/s095252380000715x
- 969 Buchanan SM, Kain JS, de Bivort BL. 2015. Neuronal control of locomotor handedness in
970 *Drosophila*. *Proc Natl Acad Sci U S A* **112**:6700–6705. doi:10.1073/pnas.1500804112
- 971 Cao L-H, Jing B-Y, Yang D, Zeng X, Shen Y, Tu Y, Luo D-G. 2016. Distinct signaling of
972 *Drosophila* chemoreceptors in olfactory sensory neurons. *Proc Natl Acad Sci U S A*
973 **113**:E902–11. doi:10.1073/pnas.1518329113
- 974 Chen T-W, Wardill TJ, Sun Y, Pulver SR, Renninger SL, Baohan A, Schreiter ER, Kerr RA,
975 Orger MB, Jayaraman V, Looger LL, Svoboda K, Kim DS. 2013. Ultrasensitive fluorescent
976 proteins for imaging neuronal activity. *Nature* **499**:295–300. doi:10.1038/nature12354
- 977 Chou Y-H, Spletter ML, Yaksi E, Leong JCS, Wilson RI, Luo L. 2010. Diversity and wiring
978 variability of olfactory local interneurons in the *Drosophila* antennal lobe. *Nat Neurosci*
979 **13**:439–449. doi:10.1038/nn.2489
- 980 Couto A, Alenius M, Dickson BJ. 2005. Molecular, anatomical, and functional organization of
981 the *Drosophila* olfactory system. *Curr Biol* **15**:1535–1547. doi:10.1016/j.cub.2005.07.034
- 982 de Bivort B, Buchanan S, Skutt-Kakaria K, Gajda E, Ayroles J, O’Leary C, Reimers P, Akhund-
983 Zade J, Senft R, Maloney R, Ho S, Werkhoven Z, Smith MA-Y. 2022. Precise
984 Quantification of Behavioral Individuality From 80 Million Decisions Across 183,000 Flies.
985 *Front Behav Neurosci* **16**:836626. doi:10.3389/fnbeh.2022.836626
- 986 de Bruyne M, Foster K, Carlson JR. 2001. Odor coding in the *Drosophila* antenna. *Neuron*

- 987 **30**:537–552. doi:10.1016/s0896-6273(01)00289-6
- 988 Dubin AE, Harris GL. 1997. Voltage-activated and odor-modulated conductances in olfactory
989 neurons of *Drosophila melanogaster*. *Journal of Neurobiology* **32**:123–137.
990 doi:10.1002/(SICI)1097-4695(199701)32:1<123::AID-NEU11>3.0.CO;2-L
- 991 Freund J, Brandmaier AM, Lewejohann L, Kirste I, Kritzler M, Krüger A, Sachser N,
992 Lindenberger U, Kempermann G. 2013. Emergence of individuality in genetically identical
993 mice. *Science* **340**:756–759. doi:10.1126/science.1235294
- 994 Gao R, Asano SM, Upadhyayula S, Pisarev I, Milkie DE, Liu T-L, Singh V, Graves A, Huynh
995 GH, Zhao Y, Bogovic J, Colonell J, Ott CM, Zugates C, Tappan S, Rodriguez A,
996 Mosaliganti KR, Sheu S-H, Pasolli HA, Pang S, Xu CS, Megason SG, Hess H, Lippincott-
997 Schwartz J, Hantman A, Rubin GM, Kirchhausen T, Saalfeld S, Aso Y, Boyden ES, Betzig
998 E. 2019. Cortical column and whole-brain imaging with molecular contrast and nanoscale
999 resolution. *Science* **363**. doi:10.1126/science.aau8302
- 1000 Golovin RM, Broadie K. 2016. Developmental experience-dependent plasticity in the first
1001 synapse of the *Drosophila* olfactory circuit. *J Neurophysiol* **116**:2730–2738.
1002 doi:10.1152/jn.00616.2016
- 1003 Gomez-Marin A, Ghazanfar AA. 2019. The Life of Behavior. *Neuron* **104**:25–36.
1004 doi:10.1016/j.neuron.2019.09.017
- 1005 Grabe V, Baschwitz A, Dweck HKM, Lavista-Llanos S, Hansson BS, Sachse S. 2016.
1006 Elucidating the Neuronal Architecture of Olfactory Glomeruli in the *Drosophila* Antennal
1007 Lobe. *Cell Rep* **16**:3401–3413. doi:10.1016/j.celrep.2016.08.063
- 1008 Grabe V, Strutz A, Baschwitz A, Hansson BS, Sachse S. 2015. Digital in vivo 3D atlas of the
1009 antennal lobe of *Drosophila melanogaster*. *J Comp Neurol* **523**:530–544.
1010 doi:10.1002/cne.23697
- 1011 Hallem EA, Ho MG, Carlson JR. 2004. The molecular basis of odor coding in the *Drosophila*
1012 antenna. *Cell* **117**:965–979. doi:10.1016/j.cell.2004.05.012
- 1013 Honegger K, de Bivort B. 2018. Stochasticity, individuality and behavior. *Curr Biol* **28**:R8–R12.
1014 doi:10.1016/j.cub.2017.11.058
- 1015 Honegger KS, Smith MA-Y, Churgin MA, Turner GC, de Bivort BL. 2019. Idiosyncratic neural
1016 coding and neuromodulation of olfactory individuality in *Drosophila*. *Proc Natl Acad Sci U*
1017 *S A*. doi:10.1073/pnas.1901623116
- 1018 Hopper KR. 1999. Risk-spreading and bet-hedging in insect population biology. *Annu Rev*
1019 *Entomol* **44**:535–560. doi:10.1146/annurev.ento.44.1.535
- 1020 Huang Y-C, Wang C-T, Su T-S, Kao K-W, Lin Y-J, Chuang C-C, Chiang A-S, Lo C-C. 2018. A
1021 Single-Cell Level and Connectome-Derived Computational Model of the *Drosophila* Brain.
1022 *Front Neuroinform* **12**:99. doi:10.3389/fninf.2018.00099
- 1023 Iyengar A, Chakraborty TS, Goswami SP, Wu C-F, Siddiqi O. 2010. Post-eclosion odor
1024 experience modifies olfactory receptor neuron coding in *Drosophila*. *Proc Natl Acad Sci U*
1025 *S A* **107**:9855–9860. doi:10.1073/pnas.1003856107
- 1026 Jeanne JM, Wilson RI. 2015. Convergence, Divergence, and Reconvergence in a Feedforward
1027 Network Improves Neural Speed and Accuracy. *Neuron* **88**:1014–1026.
1028 doi:10.1016/j.neuron.2015.10.018
- 1029 Johnson W, Turkheimer E, Gottesman II, Bouchard TJ Jr. 2010. Beyond Heritability: Twin
1030 Studies in Behavioral Research. *Curr Dir Psychol Sci* **18**:217–220. doi:10.1111/j.1467-
1031 8721.2009.01639.x
- 1032 Kain JS, Stokes C, de Bivort BL. 2012. Phototactic personality in fruit flies and its suppression

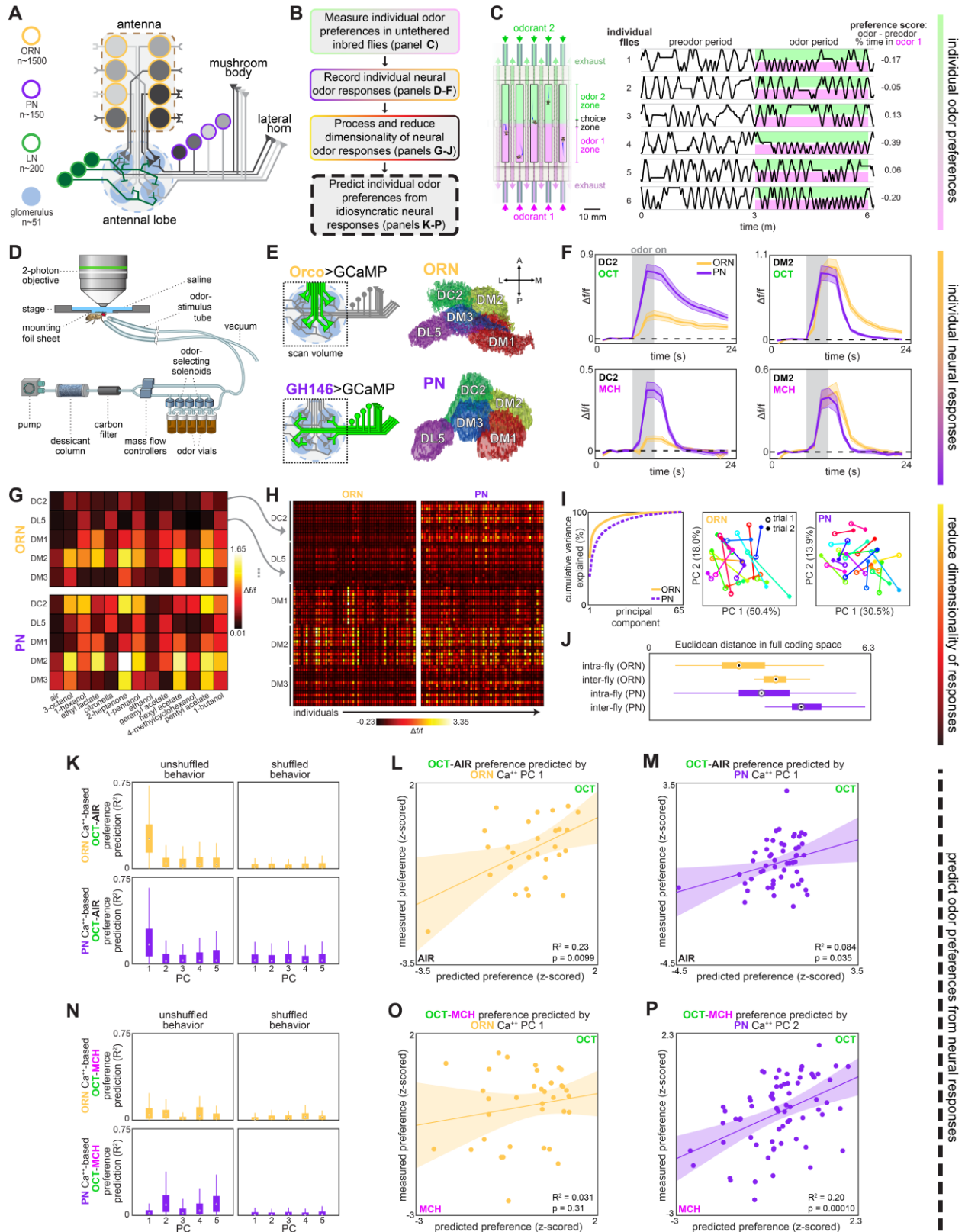
- 1033 by serotonin and white. *Proc Natl Acad Sci U S A* **109**:19834–19839.
1034 doi:10.1073/pnas.1211988109
- 1035 Kain JS, Zhang S, Akhund-Zade J, Samuel ADT, Klein M, de Bivort BL. 2015. Variability in
1036 thermal and phototactic preferences in *Drosophila* may reflect an adaptive bet-hedging
1037 strategy. *Evolution* **69**:3171–3185. doi:10.1111/evo.12813
- 1038 Kakaria KS, de Bivort BL. 2017. Ring Attractor Dynamics Emerge from a Spiking Model of the
1039 Entire Protocerebral Bridge. *Front Behav Neurosci* **11**:8. doi:10.3389/fnbeh.2017.00008
- 1040 Kao K-W, Lo C-C. 2020. Short term depression, presynaptic inhibition and local neuron
1041 diversity play key functional roles in the insect antennal lobe. *J Comput Neurosci*.
1042 doi:10.1007/s10827-020-00747-4
- 1043 Kluyver T, Ragan-Kelley B, Pérez F, Granger B, Bussonnier M, Frederic J, Kelley K, Hamrick J,
1044 Grout J, Corlay S, Ivanov P, Avila D, Abdalla S, Willing C. 2016. Jupyter Notebooks -- a
1045 publishing format for reproducible computational workflows In: Loizides F, Schmidt B,
1046 editors. Positioning and Power in Academic Publishing: Players, Agents and Agendas. IOS
1047 Press. pp. 87–90.
- 1048 Körholz JC, Zocher S, Grzyb AN, Morisse B, Poetsch A, Ehret F, Schmied C, Kempermann G.
1049 2018. Selective increases in inter-individual variability in response to environmental
1050 enrichment in female mice. *eLife* **7**. doi:10.7554/eLife.35690
- 1051 Krams IA, Krama T, Krams R, Trakimas G, Popovs S, Jöers P, Munkevics M, Elferts D, Rantala
1052 MJ, Makņa J, de Bivort BL. 2021. Serotonergic Modulation of Phototactic Variability
1053 Underpins a Bet-Hedging Strategy in *Drosophila melanogaster*. *Front Behav Neurosci*
1054 **15**:659331. doi:10.3389/fnbeh.2021.659331
- 1055 Laskowski KL, Bierbach D, Jolles JW, Doran C, Wolf M. 2022. The emergence and
1056 development of behavioral individuality in clonal fish. *Nat Commun* **13**:1–9.
1057 doi:10.1038/s41467-022-34113-y
- 1058 Li H, Horns F, Wu B, Xie Q, Li J, Li T, Luginbuhl DJ, Quake SR, Luo L. 2017. Classifying
1059 *Drosophila* Olfactory Projection Neuron Subtypes by Single-Cell RNA Sequencing. *Cell*
1060 **171**:1206–1220.e22. doi:10.1016/j.cell.2017.10.019
- 1061 Linneweber GA, Andriatsilavo M, Dutta SB, Bengochea M, Hellbruegge L, Liu G, Ejsmont RK,
1062 Straw AD, Wernet M, Hiesinger PR, Hassan BA. 2020. A neurodevelopmental origin of
1063 behavioral individuality in the *Drosophila* visual system. *Science* **367**:1112–1119.
1064 doi:10.1126/science.aaw7182
- 1065 Liu TX, Davoudian PA, Lizbinski KM, Jeanne JM. 2022. Connectomic features underlying
1066 diverse synaptic connection strengths and subcellular computation. *Curr Biol* **32**:559–
1067 569.e5. doi:10.1016/j.cub.2021.11.056
- 1068 Luo SX, Axel R, Abbott LF. 2010. Generating sparse and selective third-order responses in the
1069 olfactory system of the fly. *Proc Natl Acad Sci U S A* **107**:10713–10718.
1070 doi:10.1073/pnas.1005635107
- 1071 Maloney RT. 2021. Neuromodulation and Individuality. *Front Behav Neurosci* **15**:777873.
1072 doi:10.3389/fnbeh.2021.777873
- 1073 Marder E. 2011. Variability, compensation, and modulation in neurons and circuits. *Proc Natl*
1074 *Acad Sci U S A* **108 Suppl 3**:15542–15548. doi:10.1073/pnas.1010674108
- 1075 MATLAB pca documentation. n.d. . *MathWorks*.
1076 <https://www.mathworks.com/help/stats/pca.html>
- 1077 Mazor O, Laurent G. 2005. Transient dynamics versus fixed points in odor representations by
1078 locust antennal lobe projection neurons. *Neuron* **48**:661–673.

- 1079 doi:10.1016/j.neuron.2005.09.032
1080 McLaughlin CN, Brbić M, Xie Q, Li T, Horns F, Kolluru SS, Kebschull JM, Vacek D, Xie A, Li
1081 J, Jones RC, Leskovec J, Quake SR, Luo L, Li H. 2021. Single-cell transcriptomes of
1082 developing and adult olfactory receptor neurons in *Drosophila*. *eLife* **10**.
1083 doi:10.7554/eLife.63856
1084 Mellert DJ, Williamson WR, Shirangi TR, Card GM, Truman JW. 2016. Genetic and
1085 Environmental Control of Neurodevelopmental Robustness in *Drosophila*. *PLoS One*
1086 **11**:e0155957. doi:10.1371/journal.pone.0155957
1087 Michelson CA, Pillow JW, Seidemann E. 2017. Majority of choice-related variability in
1088 perceptual decisions is present in early sensory cortex. *bioRxiv*. doi:10.1101/207357
1089 Mosca TJ, Luo L. 2014. Synaptic organization of the *Drosophila* antennal lobe and its regulation
1090 by the Teneurins. *eLife*. doi:10.7554/elife.03726
1091 Münch D, Galizia CG. 2016. DoOR 2.0--Comprehensive Mapping of *Drosophila melanogaster*
1092 Odorant Responses. *Sci Rep* **6**:21841. doi:10.1038/srep21841
1093 Nagel KI, Hong EJ, Wilson RI. 2015. Synaptic and circuit mechanisms promoting broadband
1094 transmission of olfactory stimulus dynamics. *Nat Neurosci* **18**:56–65. doi:10.1038/nn.3895
1095 Newsome WT, Britten KH, Anthony Movshon J. 1989. Neuronal correlates of a perceptual
1096 decision. *Nature*. doi:10.1038/341052a0
1097 Olsen SR, Wilson RI. 2008. Lateral presynaptic inhibition mediates gain control in an olfactory
1098 circuit. *Nature* **452**:956–960. doi:10.1038/nature06864
1099 Osborne LC, Lisberger SG, Bialek W. 2005. A sensory source for motor variation. *Nature*
1100 **437**:412–416. doi:10.1038/nature03961
1101 Pisokas I, Heinze S, Webb B. 2020. The head direction circuit of two insect species. *eLife* **9**.
1102 doi:10.7554/eLife.53985
1103 Raj A, Rifkin SA, Andersen E, van Oudenaarden A. 2010. Variability in gene expression
1104 underlies incomplete penetrance. *Nature* **463**:913–918. doi:10.1038/nature08781
1105 Rihani K, Sachse S. 2022. Shedding Light on Inter-Individual Variability of Olfactory Circuits in
1106 *Drosophila*. *Front Behav Neurosci* **16**. doi:10.3389/fnbeh.2022.835680
1107 Rohatgi A. 2021. Webplotdigitizer: Version 4.5.
1108 Sachse S, Rueckert E, Keller A, Okada R, Tanaka NK, Ito K, Vosshall LB. 2007. Activity-
1109 dependent plasticity in an olfactory circuit. *Neuron* **56**:838–850.
1110 doi:10.1016/j.neuron.2007.10.035
1111 Scheffer LK, Xu CS, Januszewski M, Lu Z, Takemura S-Y, Hayworth KJ, Huang GB,
1112 Shinomiya K, Maitlin-Shepard J, Berg S, Clements J, Hubbard PM, Katz WT, Umayam L,
1113 Zhao T, Ackerman D, Blakely T, Bogovic J, Dolafi T, Kainmueller D, Kawase T, Khairy
1114 KA, Leavitt L, Li PH, Lindsey L, Neubarth N, Olbris DJ, Otsuna H, Trautman ET, Ito M,
1115 Bates AS, Goldammer J, Wolff T, Svirskas R, Schlegel P, Neace E, Knecht CJ, Alvarado
1116 CX, Bailey DA, Ballinger S, Borycz JA, Canino BS, Cheatham N, Cook M, Dreher M,
1117 Duclos O, Eubanks B, Fairbanks K, Finley S, Forknall N, Francis A, Hopkins GP, Joyce
1118 EM, Kim S, Kirk NA, Kovalyak J, Lauchie SA, Lohff A, Maldonado C, Manley EA, McLin
1119 S, Mooney C, Ndama M, Ogundeyi O, Okeoma N, Ordish C, Padilla N, Patrick CM,
1120 Paterson T, Phillips EE, Phillips EM, Rampally N, Ribeiro C, Robertson MK, Rymer JT,
1121 Ryan SM, Sammons M, Scott AK, Scott AL, Shinomiya A, Smith C, Smith K, Smith NL,
1122 Sobeski MA, Suleiman A, Swift J, Takemura S, Talebi I, Tarnogorska D, Tenshaw E, Tokhi
1123 T, Walsh JJ, Yang T, Horne JA, Li F, Parekh R, Rivlin PK, Jayaraman V, Costa M, Jefferis
1124 GS, Ito K, Saalfeld S, George R, Meinertzhagen IA, Rubin GM, Hess HF, Jain V, Plaza

- 1125 SM. 2020. A connectome and analysis of the adult *Drosophila* central brain. *eLife* **9**.
1126 doi:10.7554/eLife.57443
- 1127 Schlegel P, Bates AS, Stürner T, Jagannathan S, Drummond N, Hsu J, Capdevila LS, Javier A,
1128 Marin EC, Barth-Maron A, Tamimi IFM, Li F, Rubin GM, Plaza SM, Costa M, Jefferis
1129 GSXE. 2020. Information flow, cell types and stereotypy in a full olfactory connectome.
1130 *bioRxiv*. doi:10.1101/2020.12.15.401257
- 1131 Schuett W, Dall SRX, Baeumer J, Kloesener MH, Nakagawa S, Beinlich F, Eggers T. 2011.
1132 Personality variation in a clonal insect: the pea aphid, *Acyrtosiphon pisum*. *Dev*
1133 *Psychobiol* **53**:631–640. doi:10.1002/dev.20538
- 1134 Seki Y, Rybak J, Wicher D, Sachse S, Hansson BS. 2010. Physiological and morphological
1135 characterization of local interneurons in the *Drosophila* antennal lobe. *J Neurophysiol*
1136 **104**:1007–1019. doi:10.1152/jn.00249.2010
- 1137 Shang Y, Claridge-Chang A, Sjulson L, Pypaert M, Miesenböck G. 2007. Excitatory local
1138 circuits and their implications for olfactory processing in the fly antennal lobe. *Cell*
1139 **128**:601–612. doi:10.1016/j.cell.2006.12.034
- 1140 Sizemore TR, Dacks AM. 2016. Serotonergic Modulation Differentially Targets Distinct
1141 Network Elements within the Antennal Lobe of *Drosophila melanogaster*. *Sci Rep* **6**:37119.
1142 doi:10.1038/srep37119
- 1143 Skutt-Kakaria K, Reimers P, Currier TA, Werkhoven Z, de Bivort BL. 2019. A neural circuit
1144 basis for context-modulation of individual locomotor behavior. *bioRxiv*.
1145 doi:10.1101/797126
- 1146 Stern S, Kirst C, Bargmann CI. 2017. Neuromodulatory Control of Long-Term Behavioral
1147 Patterns and Individuality across Development. *Cell* **171**:1649–1662.e10.
1148 doi:10.1016/j.cell.2017.10.041
- 1149 Tobin WF, Wilson RI, Lee W-CA. 2017. Wiring variations that enable and constrain neural
1150 computation in a sensory microcircuit. *eLife* **6**:e24838. doi:10.7554/eLife.24838
- 1151 Tsai K-T, Hu C-K, Li K-W, Hwang W-L, Chou Y-H. 2018. Circuit variability interacts with
1152 excitatory-inhibitory diversity of interneurons to regulate network encoding capacity. *Sci*
1153 *Rep* **8**:8027. doi:10.1038/s41598-018-26286-8
- 1154 van Rossum G, Drake FL. 2011. The Python Language Reference Manual. Network Theory Ltd.
1155 Werkhoven Z, Bravin A, Skutt-Kakaria K, Reimers P, Pallares LF, Ayroles J, de Bivort BL.
1156 2021. The structure of behavioral variation within a genotype. *eLife* **10**:e64988.
1157 doi:10.7554/eLife.64988
- 1158 Wilson RI. 2013. Early Olfactory Processing in *Drosophila*: Mechanisms and Principles. *Annual*
1159 *Review of Neuroscience*. doi:10.1146/annurev-neuro-062111-150533
- 1160 Wilson RI. 2004. Transformation of Olfactory Representations in the *Drosophila* Antennal Lobe.
1161 *Science*. doi:10.1126/science.1090782
- 1162 Wilson RI, Laurent G. 2005. Role of GABAergic inhibition in shaping odor-evoked
1163 spatiotemporal patterns in the *Drosophila* antennal lobe. *J Neurosci* **25**:9069–9079.
1164 doi:10.1523/JNEUROSCI.2070-05.2005
- 1165 Wilson RI, Turner GC, Laurent G. 2004. Transformation of olfactory representations in the
1166 *Drosophila* antennal lobe. *Science* **303**:366–370. doi:10.1126/science.1090782
- 1167 Wu JS, Luo L. 2006. A protocol for dissecting *Drosophila melanogaster* brains for live imaging
1168 or immunostaining. *Nat Protoc* **1**:2110–2115. doi:10.1038/nprot.2006.336
- 1169 Xie Q, Brbic M, Horns F, Kolluru SS, Jones RC, Li J, Reddy AR, Xie A, Kohani S, Li Z,
1170 McLaughlin CN, Li T, Xu C, Vacek D, Luginbuhl DJ, Leskovec J, Quake SR, Luo L, Li H.

- 1171 2021. Temporal evolution of single-cell transcriptomes of *Drosophila* olfactory projection
1172 neurons. *eLife* **10**. doi:10.7554/eLife.63450
1173 Yaksi E, Wilson RI. 2010. Electrical coupling between olfactory glomeruli. *Neuron* **67**:1034–
1174 1047. doi:10.1016/j.neuron.2010.08.041
1175 Zocher S, Schilling S, Grzyb AN, Adusumilli VS, Bogado Lopes J, Günther S, Overall RW,
1176 Winter Y, Kempermann G. 2020. Early-life environmental enrichment generates persistent
1177 individualized behavior in mice. *Sci Adv* **6**:eabb1478. doi:10.1126/sciadv.abb1478

1178 **Figures and figure supplements**



1179

1180

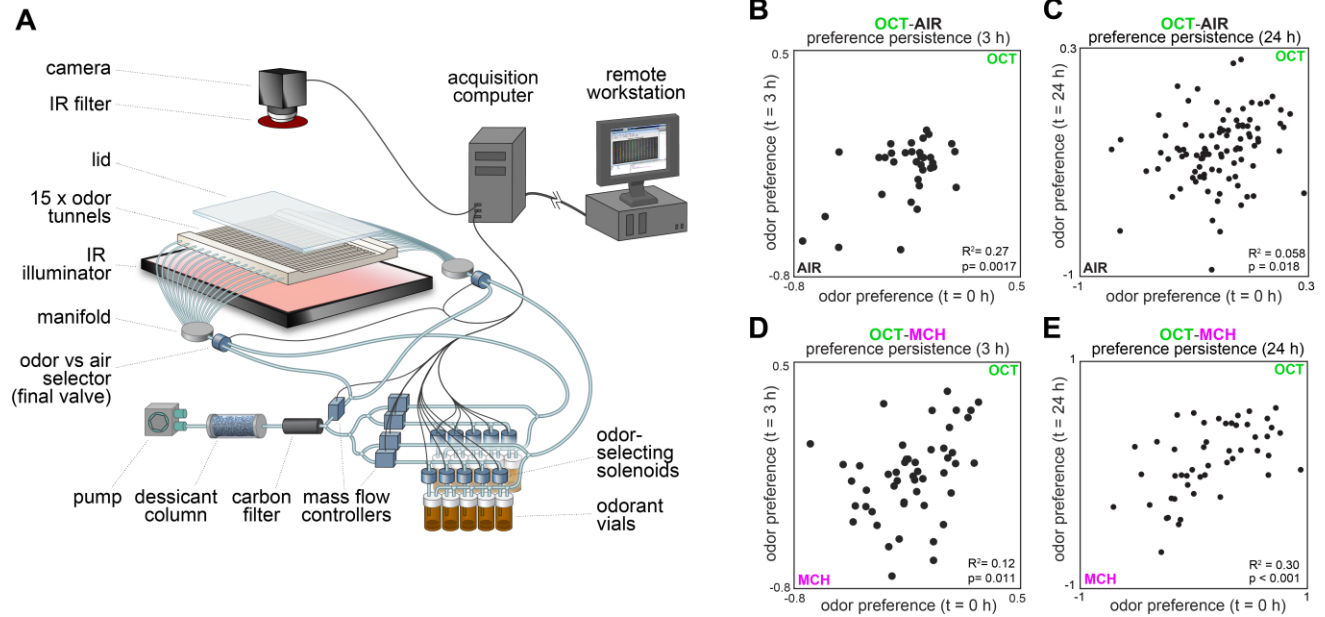
1181

1182

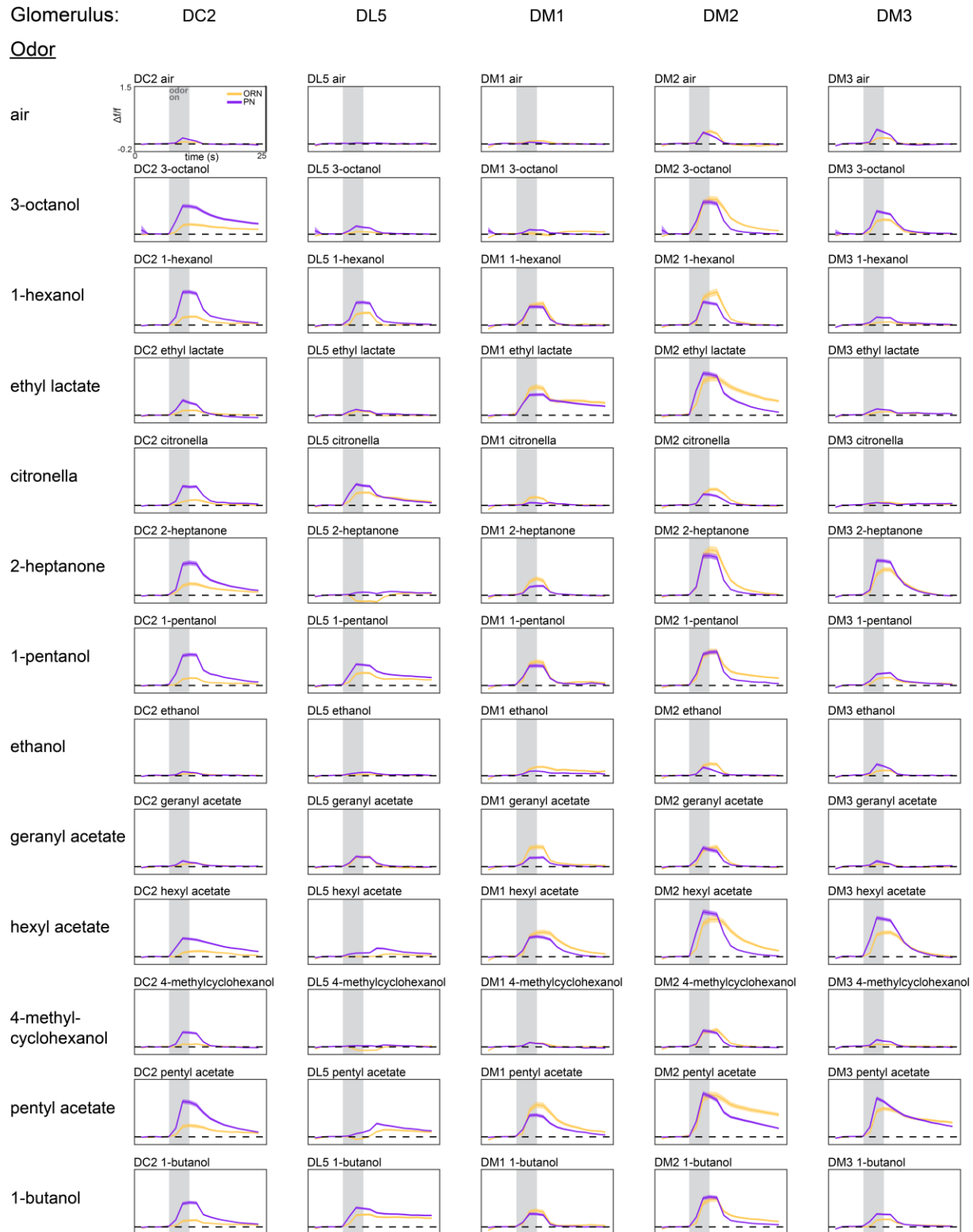
Figure 1. Idiosyncratic calcium dynamics predict individual odor preferences.

(A) Olfactory circuit schematic. Olfactory receptor neurons (ORNs, peach outline) and projection neurons (PNs, plum outline) are comprised of ~51 classes corresponding to odor

1183 receptor response channels. ORNs (gray shading) sense odors in the antennae and synapse on
1184 dendrites of PNs of the same class in ball-shaped structures called glomeruli located in the
1185 antennal lobe (AL). Local neurons (LNs, green outline) mediate interglomerular cross-talk and
1186 presynaptic inhibition, amongst other roles (Olsen and Wilson, 2008; Yaksi and Wilson, 2010).
1187 Odor signals are normalized and whitened in the AL before being sent to the mushroom body
1188 and lateral horn for further processing. Schematic adapted from Honegger et al., 2019 **(B)**
1189 Experiment outline. **(C)** Odor preference behavior tracking setup (reproduced from Honegger,
1190 Smith, et al. (Honegger et al., 2019)) and example individual fly ethograms. OCT (green) and
1191 MCH (magenta) were presented for 3 minutes. **(D)** Head-fixed 2-photon calcium imaging and
1192 odor delivery setup (reproduced from Honegger et al., 2019) **(E)** Orco and GH146 driver
1193 expression profiles (left) and example segmentation masks (right) extracted from 2-photon
1194 calcium images for a single fly expressing Orco>GCaMP6m (top, expressed in a subset of all
1195 ORN classes) or GH146>Gcamp6m (bottom, expressed in a subset of all PN classes). **(F)** Time-
1196 dependent $\Delta f/f$ for glomerular odor responses in ORNs (peach) and PNs (plum) averaged across
1197 all individuals: DC2 to OCT (upper left), DM2 to OCT (upper right), DC2 to MCH (lower left),
1198 and DM2 to OCT (lower right). Shaded error bars represent S.E.M. **(G)** Peak $\Delta f/f$ for each
1199 glomerulus-odor pair averaged across all flies. **(H)** Individual neural responses measured in
1200 ORNs (left) or PNs (right) for 50 flies each. Columns represent the average of up to 4 odor
1201 responses from a single fly. Each row represents one glomerulus-odor response pair. Odors are
1202 the same as in panel (G). **(I)** Principal component analysis of individual neural responses.
1203 Fraction of variance explained versus principal component number (left). Trial 1 and trial 2 of
1204 ORN (middle) and PN (right) responses for 20 individuals (unique colors) embedded in PC 1-2
1205 space. **(J)** Euclidean distances between glomerulus-odor responses within and across flies
1206 measured in ORNs (n=65 flies) and PNs (n=122 flies). Distances calculated without PCA
1207 compression. Points represent the median value, boxes represent the interquartile range, and
1208 whiskers the range of the data. **(K)** Bootstrapped R^2 of OCT-AIR preference prediction from
1209 each of the first 5 principal components of neural activity measured in ORNs (top, all data) or
1210 PNs (bottom, training set). **(L)** Measured OCT-AIR preference versus preference predicted from
1211 PC 1 of ORN activity (n=30 flies). **(M)** Measured OCT-AIR preference versus preference
1212 predicted from PC 1 of PN activity in n=53 flies using a model trained on a training set of n=18
1213 flies (see Figure 2 – figure supplement 1A-B for train/test flies analyzed separately). **(N)**
1214 Bootstrapped R^2 of OCT-MCH preference prediction from each of the first 5 principal
1215 components of neural activity measured in ORNs (top, all data) or PNs (bottom, training set).
1216 **(O)** Measured OCT-MCH preference versus preference predicted from PC 1 of ORN activity
1217 (n=35 flies). **(P)** Measured OCT-MCH preference versus preference predicted from PC 2 of PN
1218 activity in n=69 flies using a model trained on a training set of n=47 flies (see Figure 2 – figure
1219 supplement 1C-D for train/test flies analyzed separately). Shaded regions in L,M,O,P are the
1220 95% CI of the fit estimated by bootstrapping.

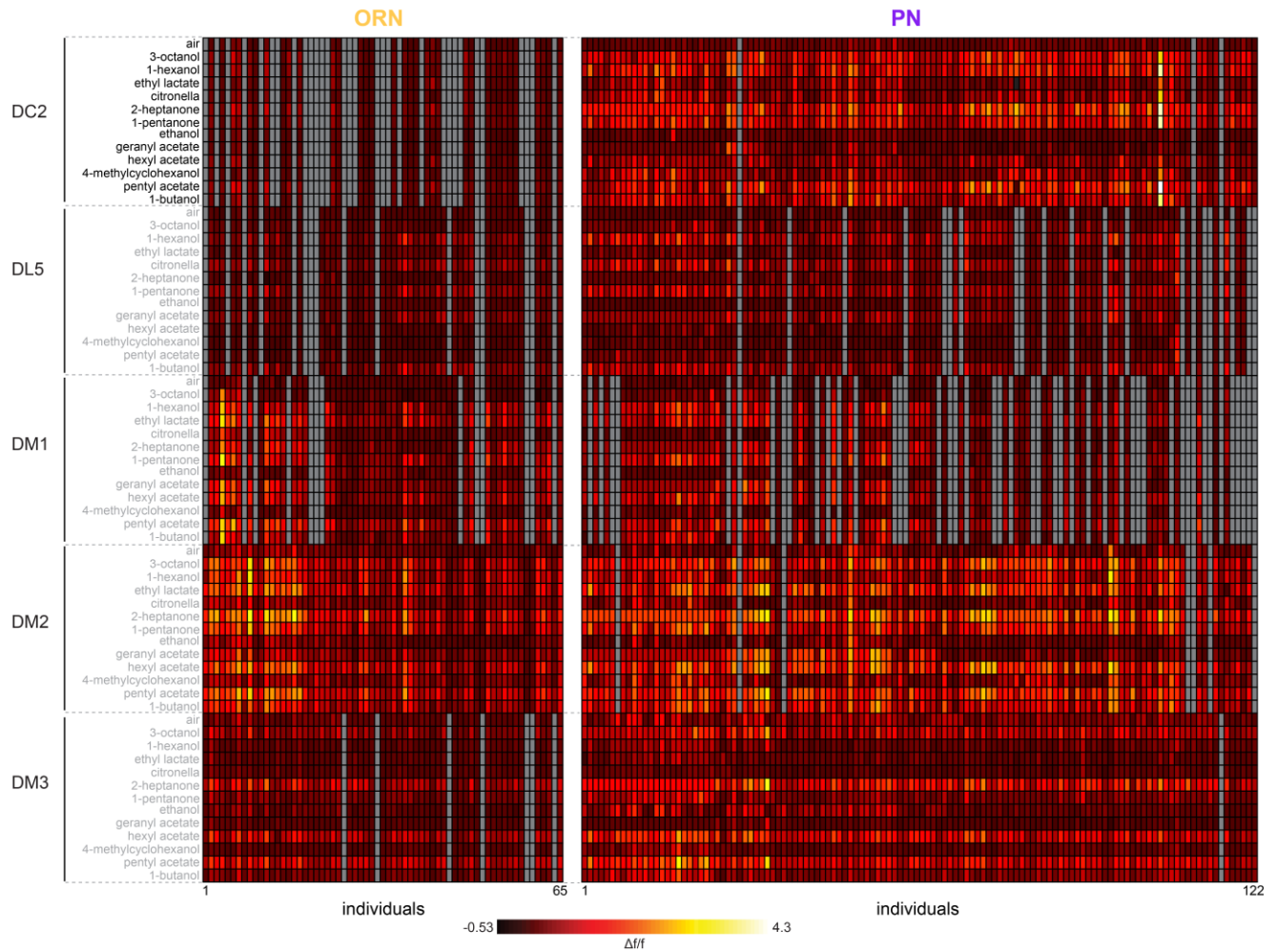


1221
1222 **Figure 1 – figure supplement 1. Behavioral measurements and individual preference**
1223 **persistence.**
1224 **(A)** Behavioral measurement apparatus (adapted from Honegger et al., 2019) **(B)** Odor
1225 preference persistence over 3 hours for flies given a choice between 3-octanol and air (n=34
1226 flies). **(C)** Odor preference persistence over 24 hours for flies given a choice between 3-octanol
1227 and air (n=97 flies). **(D)** Odor preference persistence over 3 hours for flies given a choice
1228 between 3-octanol and 4-methylcyclohexanol (n=51 flies). **(E)** Odor preference persistence over
1229 24 hours for flies given a choice between 3-octanol and 4-methylcyclohexanol (n=49 flies).



1230
1231
1232
1233
1234

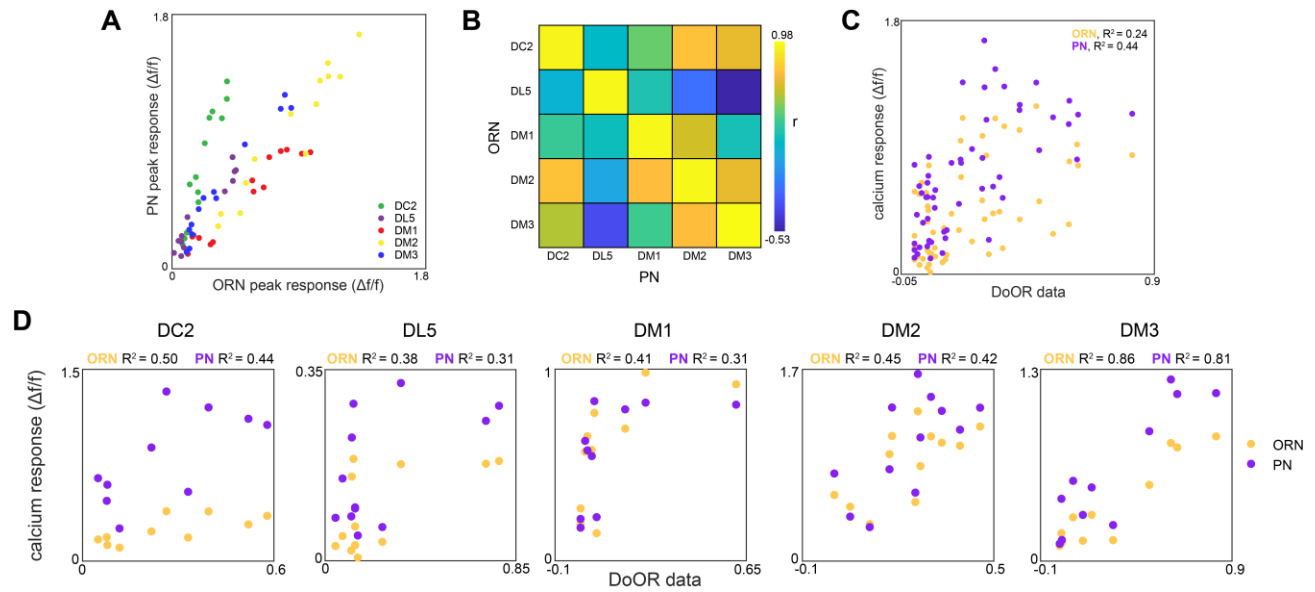
Figure 1 – figure supplement 2. Average glomerulus-odor time-dependent responses. Time-dependent responses of each glomerulus identified in our study to the 13 odors in our odor panel. Data represents the average across flies (ORN, peach curves, n=65 flies; PN, plum curves, n=122 flies). Shaded error bars represent S.E.M.



1235
1236
1237
1238
1239
1240

Figure 1 – figure supplement 3. Individual glomerulus-odor responses.

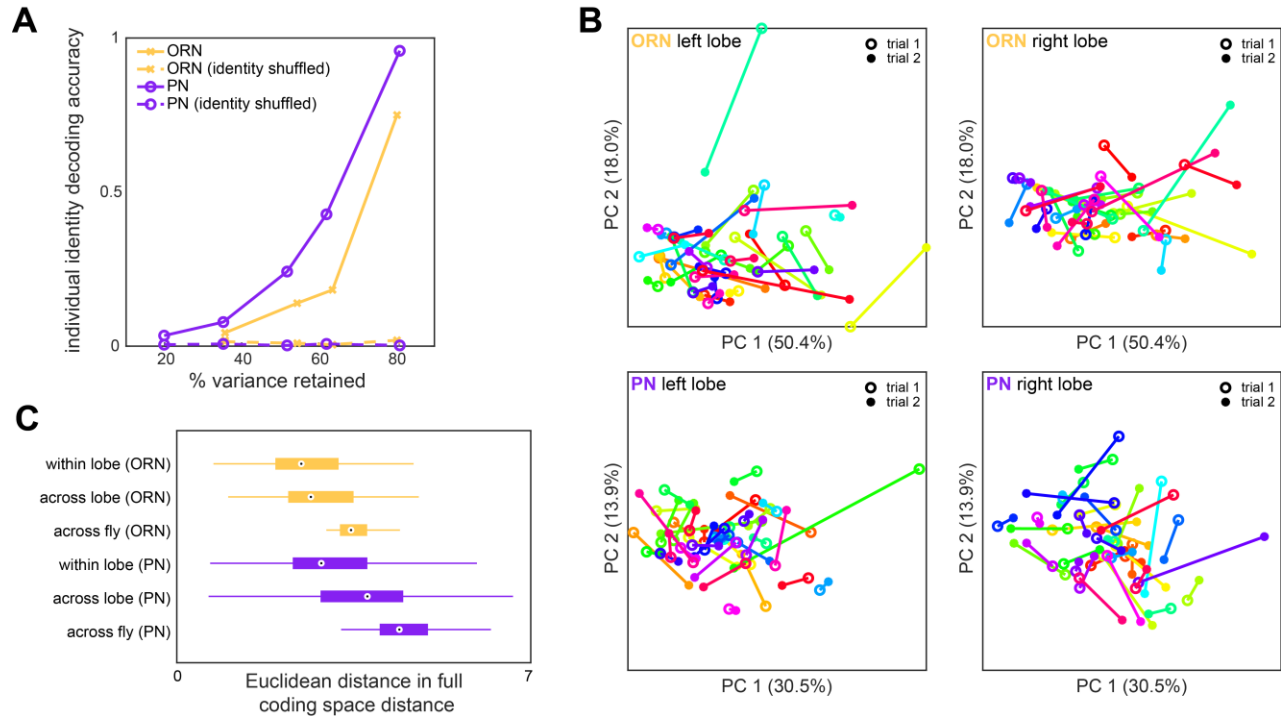
Idiosyncratic odor coding measured in ORNs (left, n=65 flies) and PNs (right, n=122 flies). Each column represents the response (max $\Delta f/f$ attained over the odor trial) of a single fly averaged over up to 4 odor deliveries. Each row represents a glomerulus-odor response pair. Missing data are indicated in gray.



1241
1242
1243
1244
1245
1246
1247
1248

Figure 1 – figure supplement 4. Glomerulus responses and identification.

(A) Glomerulus odor responses measured in PNs versus those measured in ORNs. Points correspond to the odorants listed in Figure 1G. (B) Cross-odor trial correlation matrix between glomerular odor responses in ORNs and PNs. (C) Peak calcium responses for each glomerulus-odor pair measured in this study plotted against those recorded in the DoOR dataset (Münch and Galizia, 2016). (D) Peak calcium responses for each individual glomerulus plotted against those recorded in the DoOR dataset.



1249

1250

Figure 1 – figure supplement 5. Idiosyncrasy of ORN and PN responses.

1251

(A) Logistic regression classifier accuracy of decoding individual identity from individual odor panel peak responses. PCA was performed on population responses and the specified fraction of variance (x-axis) was retained. Individual identity can be better decoded from PN responses than ORN responses in all cases. (B) Individual trial-to-trial glomerulus-odor responses embedded in PC 1-2 space. Responses for the same flies as Figure 1I are shown. Each linked color represents one fly. Trial 1 and trial 2 responses are shown for ORN left lobe (upper left), ORN right lobe (upper right), PN left lobe (lower left), and PN right lobe (lower right). (C) Distance in the full glomerulus-odor response space between recordings within a lobe (trial-to-trial), across lobes (within fly), and across flies for ORNs and PNs. Points represent the median value, boxes represent the interquartile range, and whiskers the range of the data.

1252

1253

1254

1255

1256

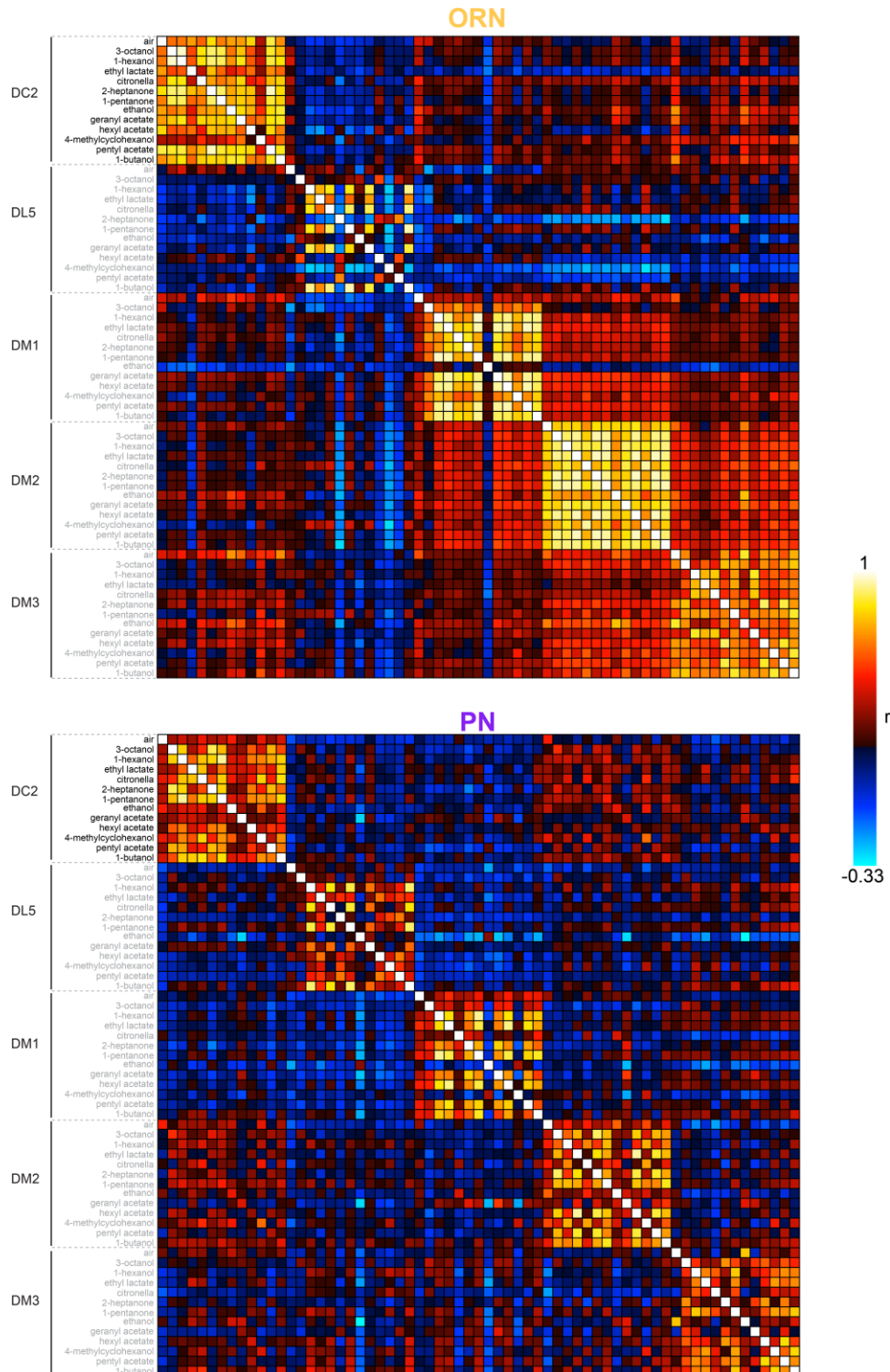
1257

1258

1259

1260

1261



1262

1263

1264

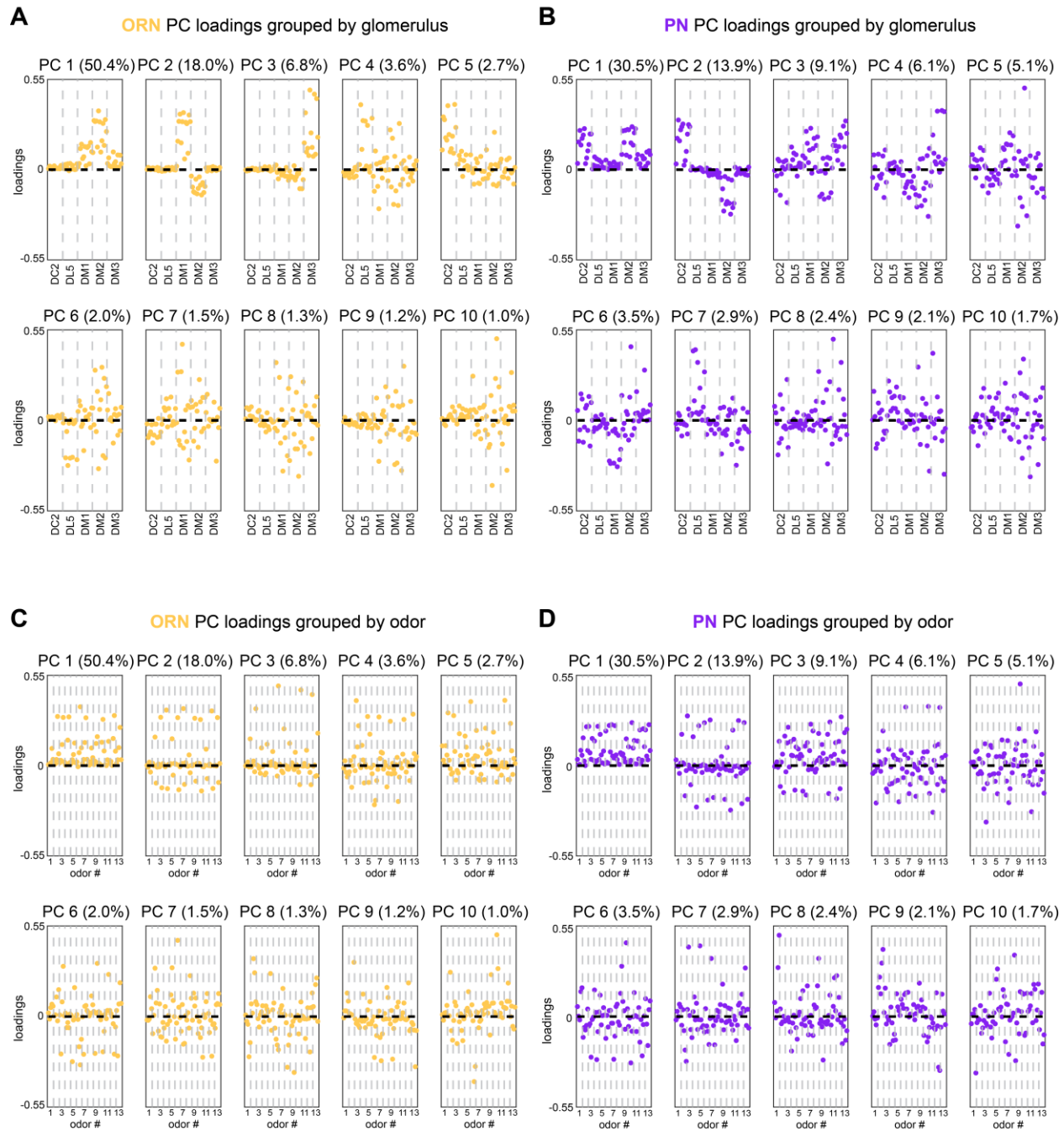
1265

1266

1267

Figure 1 – figure supplement 6. Calcium response correlation matrices.

Correlation between calcium response dimensions across flies measured in ORNs (top) and PNs (bottom). Glomerulus-odor responses are correlated at the level of glomeruli in both cell types. Inter-glomerulus correlations are more prominent in ORNs than PNs, consistent with known AL transformations that result in decorrelated PN activity (Bhandawat et al., 2007; Luo et al., 2010).



1268

1269

1270

1271

1272

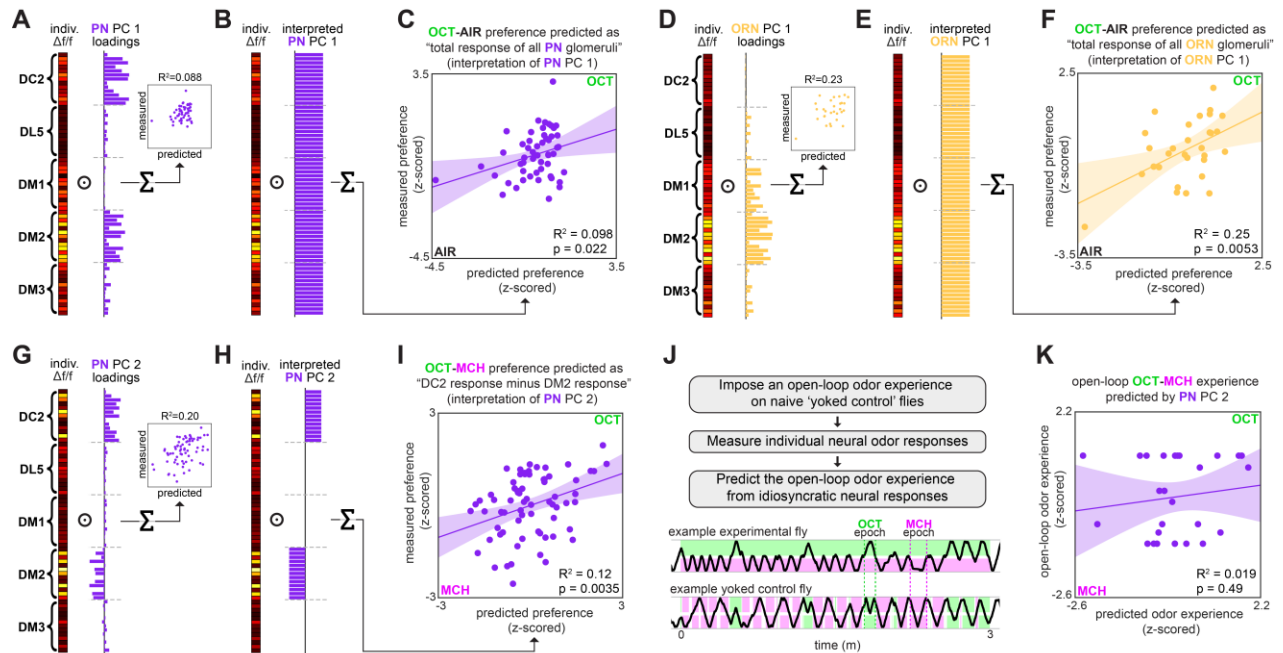
1273

1274

1275

Figure 1 – figure supplement 7. Calcium imaging principal component loadings.

(A-B) First 10 principal component loadings measured from calcium responses in ORNs (A, n=65 flies) and PNs (B, n=122 flies). Loadings are grouped by glomerulus, with each loading within a glomerulus representing the response of that glomerulus to one odor in the odor panel. Odors are the same as those listed in Figure 1G. (C-D) The same 10 principal component loadings as those shown in panels (A-B) grouped by odor rather than glomerulus. Glomeruli within each odor block are given in the order of panels (A) and (B).



1276

1277

1278

Figure 2. Variation in global and relative glomerular responses explains individual preferences.

1279

1280

1281

1282

1283

1284

1285

1286

1287

1288

1289

1290

1291

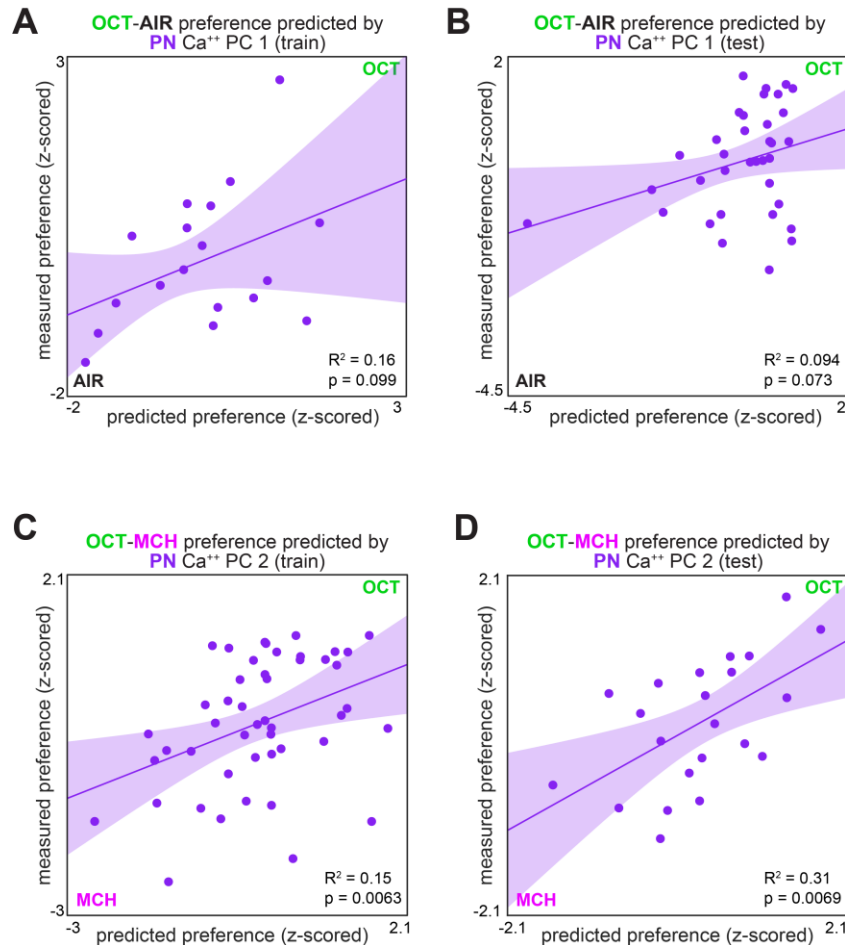
1292

1293

1294

(A) PC 1 loadings of PN activity for flies tested for OCT-AIR preference (n=53 flies). (B) Interpreted PN PC 1 loadings. (C) Measured OCT-AIR preference versus preference predicted by the average peak response across all PN coding dimensions (n=53 flies). (D) PC 1 loadings of ORN activity for flies tested for OCT-AIR preference (n=30 flies). (E) Interpreted ORN PC 1 loadings. (F) Measured OCT-AIR preference versus preference predicted by the average peak response across all ORN coding dimensions (n=30 flies). (G) PC 2 loadings of PN activity for flies tested for OCT-MCH preference (n=69 flies). (H) Interpreted PN PC 2 loadings. (I) Measured OCT-MCH preference versus preference predicted by the average peak PN response in DM2 minus DC2 across all odors (n=69 flies). (J) Yoked control experiment outline and example behavior traces. Experimental flies are free to move about tunnels permeated with steady state OCT and MCH flowing into either end. Yoked control flies are delivered the same odor at both ends of the tunnel which matches the odor experienced at the nose of the experimental fly at each moment in time. (K) Imposed odor experience versus the odor experience predicted from PC 2 of PN activity (n=27 flies) evaluated on the model trained from data in Figure 1P. Shaded regions in C,F,I,K are the 95% CI of the fit estimated by bootstrapping.

1295



1296

1297

1298

1299

1300

1301

1302

1303

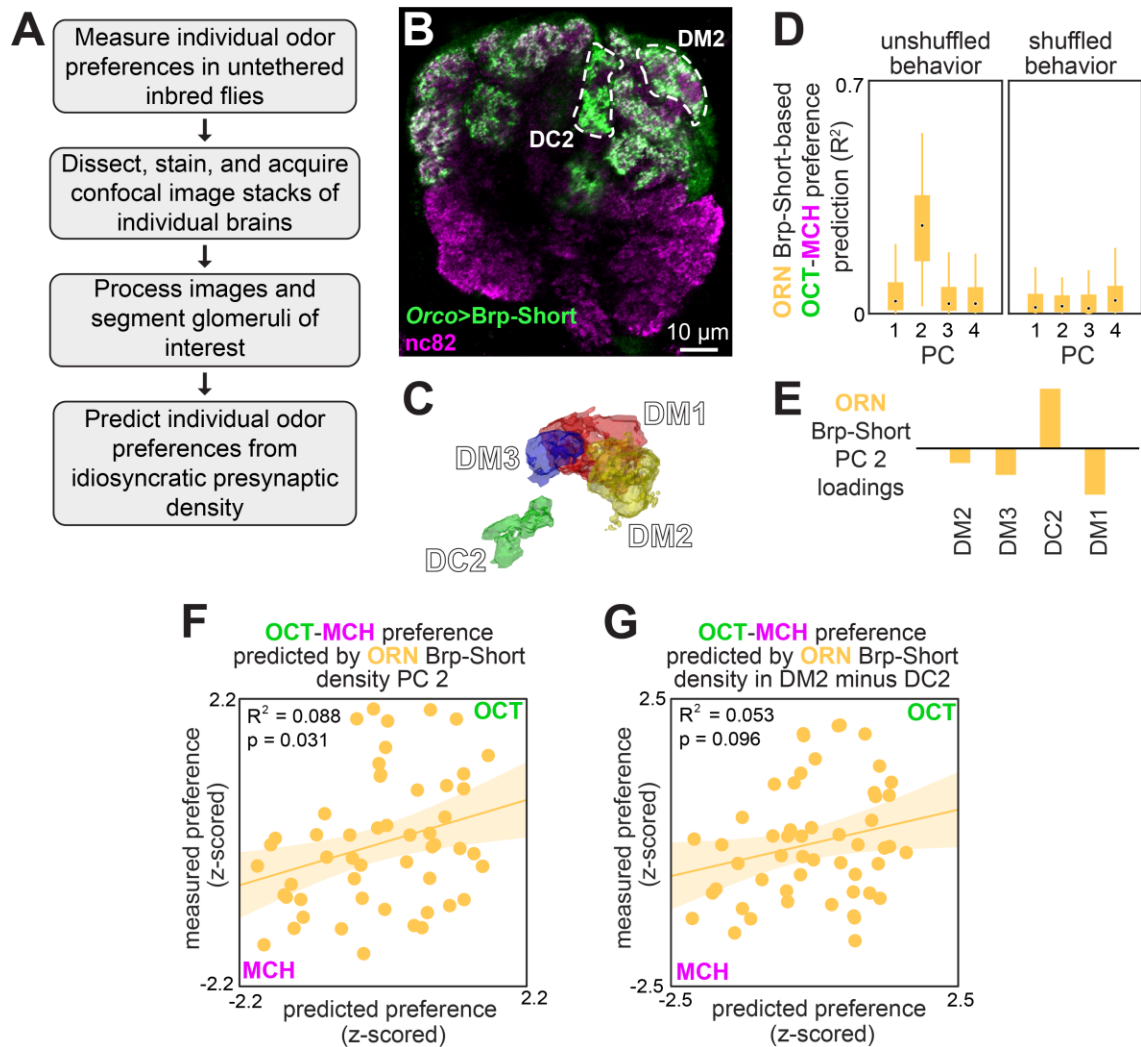
1304

1305

Figure 2 – figure supplement 1. Measured preference vs. PN activity-based predicted preference, split by training/testing set.

(A) Measured OCT-AIR preference versus preference predicted from PC 1 of PN activity in a training set (n=18 flies). (B) Measured OCT-AIR preference versus preference predicted from PC 1 on PN activity in a test set (n=35 flies) evaluated on a model trained on data from panel (A). (C) Measured OCT-MCH preference versus preference predicted from PC 2 of PN activity in a training set (n=47 flies). (D) Measured OCT-MCH preference versus preference predicted from PC 2 on PN activity in a test set (n=22 flies) evaluated on a model trained on data from panel (C).

1306



1307

1308

1309

1310

1311

1312

1313

1314

1315

1316

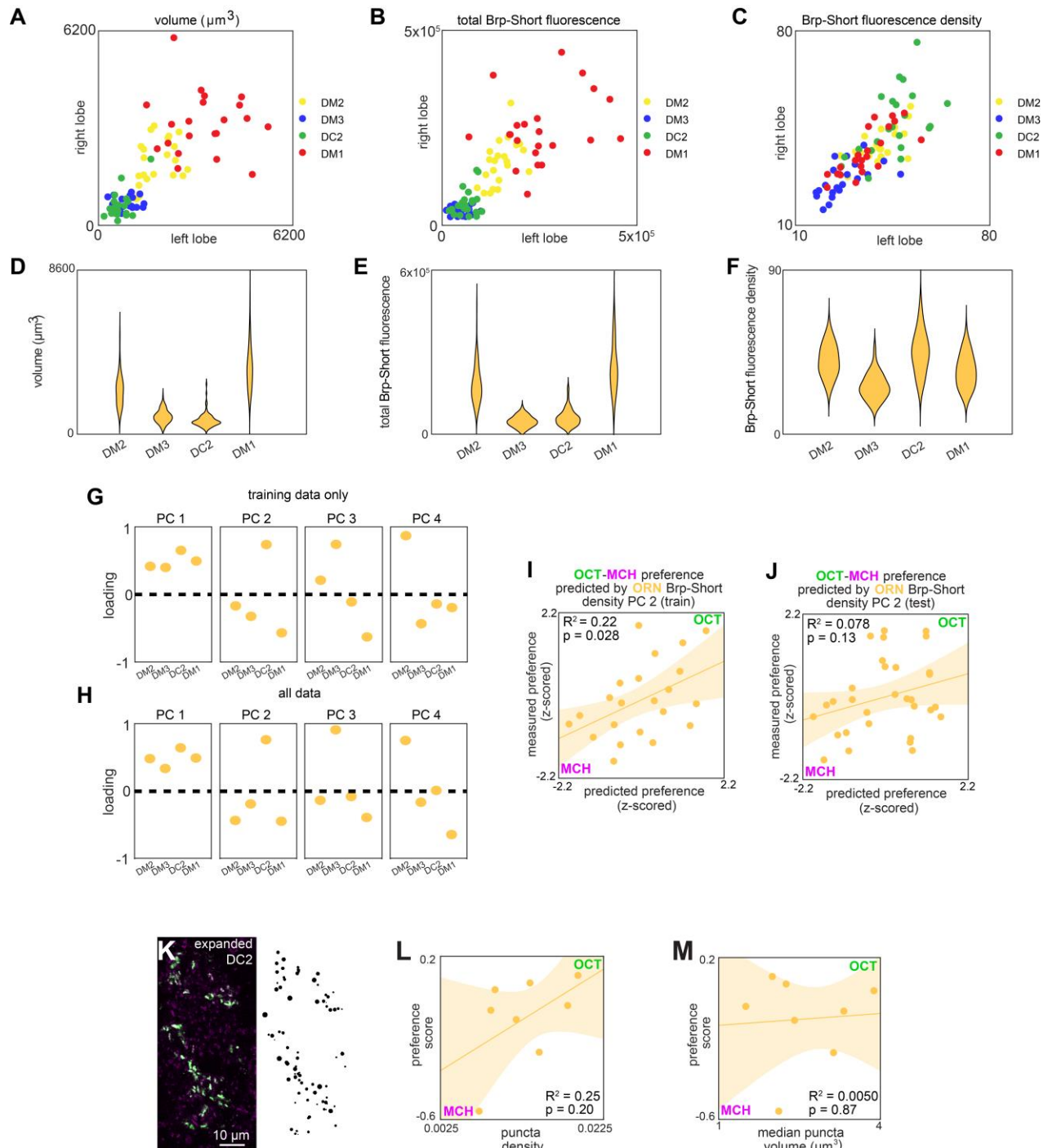
1317

1318

1319

Figure 3. Idiosyncratic presynaptic marker density in DM2 and DC2 predicts OCT-MCH preference.

(A) Experiment outline. (B) Example slice from a z-stack of the antennal lobe expressing Orco>Brp-Short (green) with DC2 and DM2 visible (white dashed outline). nc82 counterstain (magenta). (C) Example glomerulus segmentation masks extracted from an individual z-stack. (D) Bootstrapped R^2 of OCT-MCH preference prediction from each of the first 4 principal components of Brp-Short density measured in ORNs (training set, $n=22$ flies). (E) PC 2 loadings of Brp-Short density. (F) Measured OCT-MCH preference versus preference predicted from PC 2 of ORN Brp-Short density in $n=53$ flies using a model trained on a training set of $n=22$ flies (see Figure 3 – figure supplement 1 for train/test flies analyzed separately). (G) Measured OCT-MCH preference versus preference predicted from ORN Brp-Short density in DM2 minus DC2 ($n=53$ flies).

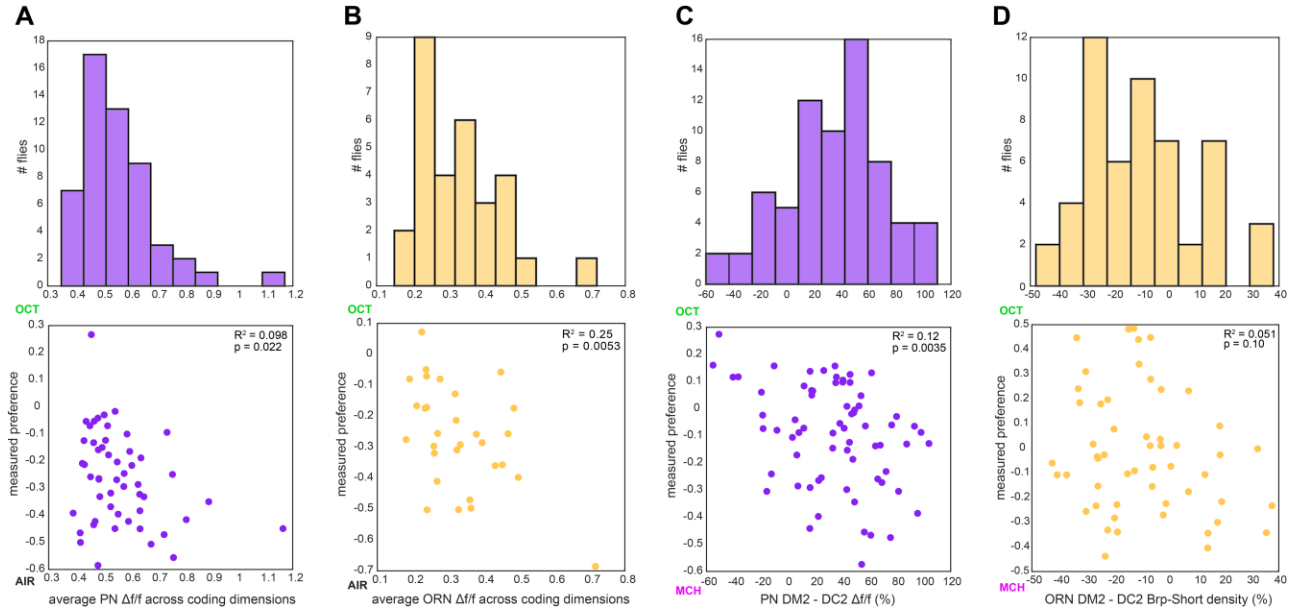


1320
1321
1322
1323
1324
1325
1326
1327
1328

Figure 3 – figure supplement 1. ORN>Brp-Short characterization and model predictions.

(A-C) Right versus left glomerulus properties measured from z-stacks of stained Orco>Brp-Short samples: (A) Volume, (B) total Brp-Short fluorescence, (C) Brp-Short fluorescence density. (D-F) Same data as panels (A-C) represented in violin plots (kernel density estimated). (G) Principal component loadings of Brp-Short density calculated using only training data (n=22 flies). (H) Principal component loadings of Brp-Short density calculated using all data (n=53 flies). (I) Measured OCT-MCH preference versus preference predicted from PC 2 of ORN Brp-Short density in a training set (n=22 flies). (J) Measured OCT-MCH preference versus

1329 preference predicted from PC 2 on ORN Brp-Short density in a test set (n=31 flies) evaluated on
1330 a model trained on data from panel (I). **(K)** Example expanded AL expressing Or13a>Brp-Short
1331 (left) and Imaris-identified puncta from that sample (right). **(L)** OCT-MCH preference score
1332 plotted against Brp-Short puncta density in expanded Or13a>Brp-Short samples (n=8 flies). **(M)**
1333 OCT-MCH preference score plotted against Brp-Short median puncta volume in expanded
1334 Or13a>Brp-Short samples (n=8 flies). Shaded regions in F,G,I,J are the 95% CI of the fit
1335 estimated by bootstrapping.



1336

1337

1338

1339

1340

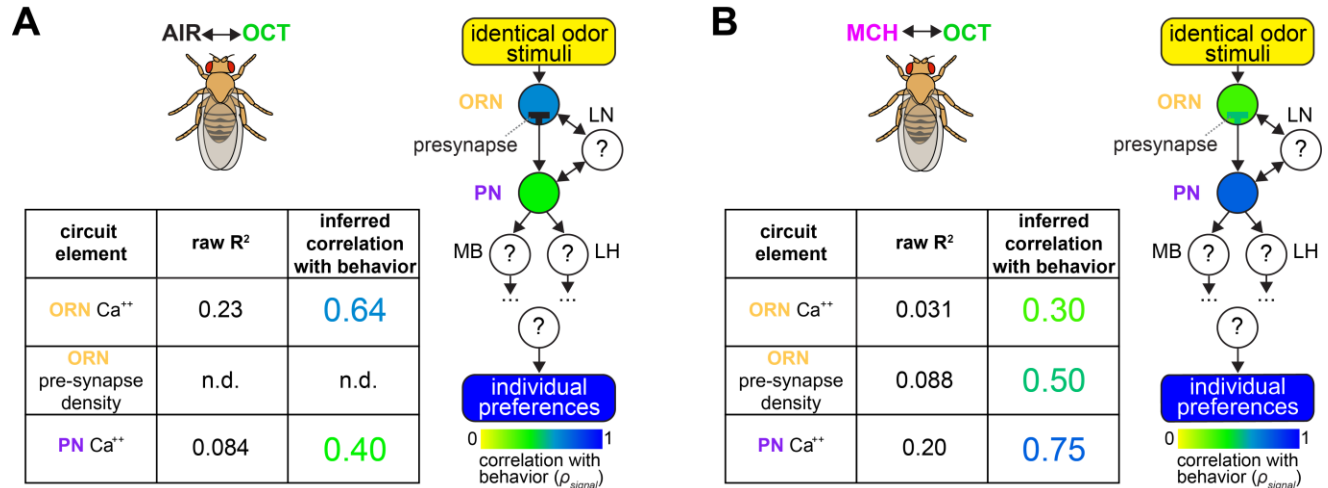
1341

1342

1343

Figure 3 – figure supplement 2. Calcium and Brp-Short predictor variation.

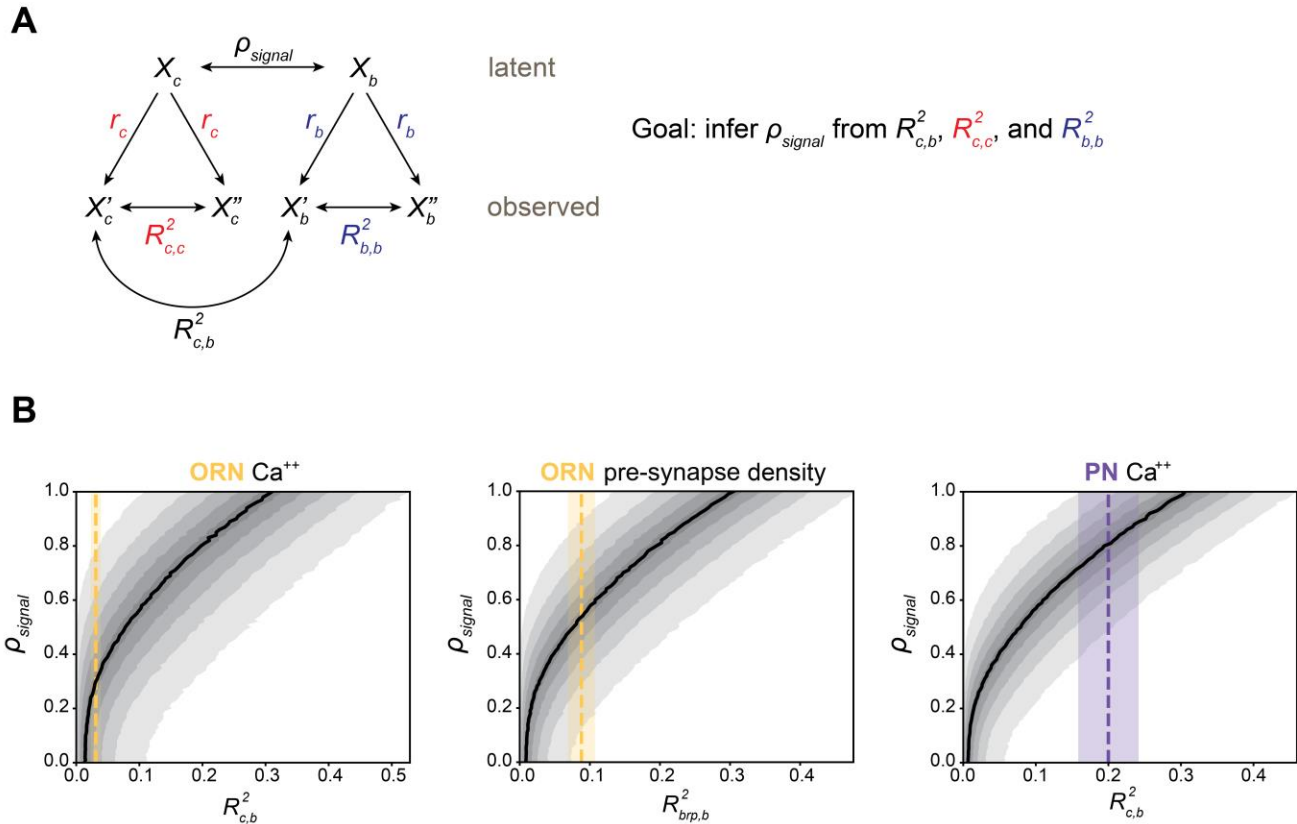
(A) Histogram of average PN $\Delta f/f$ across all coding dimensions in flies in which OCT-AIR preference was measured (top) and OCT-AIR preference versus average PN $\Delta f/f$ (n=53 flies) (bottom). (B) Similar to (A) for ORN $\Delta f/f$ and OCT-AIR preference (n=30 flies). (C) Similar to (A) for $\Delta f/f$ difference between DM2 and DC2 PN responses and OCT-MCH preference (n=69 flies). (D) Similar to (A) for % Brp-Short density difference between DM2 and DC2 ORNs and OCT-MCH (n=53 flies).



1344
1345
1346
1347
1348
1349
1350
1351
1352
1353
1354

Figure 4. Loci of individuality across the olfactory periphery.

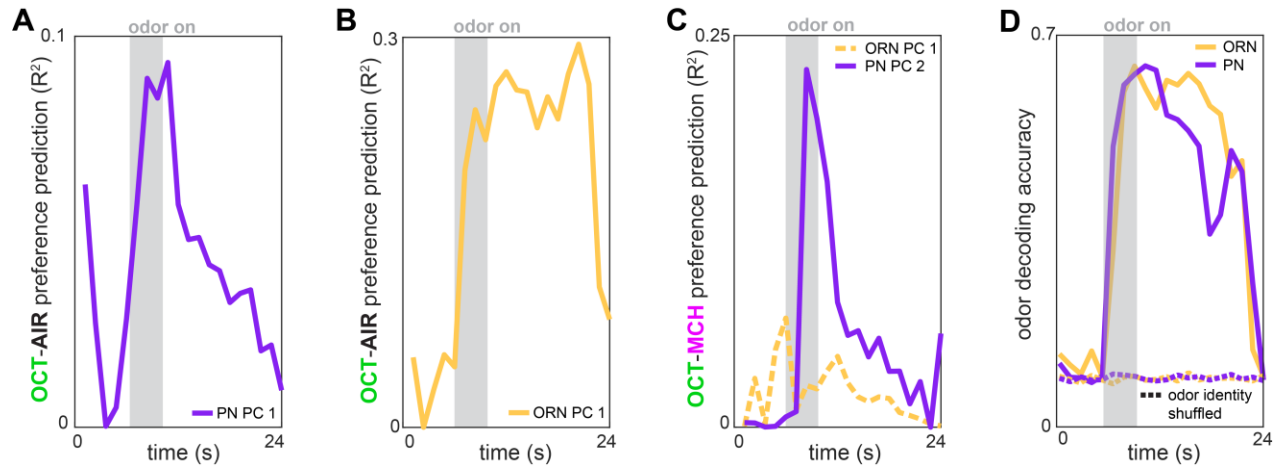
(A) Table summarizing circuit element predictors, the strength of their nominal correlation with odor-vs-air behavior scores, and the inferred correlation between latent calcium / latent behavior. See analysis in Figure 4 – figure supplement 1. Schematic at right places these values in the context of the olfactory circuit. ORN Ca⁺⁺ corresponds to PC 1 of ORN calcium (Figure 1L), PN Ca⁺⁺ corresponds to PC1 of PN calcium (Figure 1M; trained model applied to train+test data). (B) As in (A) but for odor-vs-odor experiments. ORN Ca⁺⁺ corresponds to PC 1 of ORN calcium (Figure 1O), ORN pre-synapse density corresponds to PC2 of Brp-Short relative fluorescence (Figure 3F; trained model applied to train+test data), PN Ca⁺⁺ corresponds to PC 2 of PN calcium (Figure 1P; trained model applied to train+test data).



1355
1356
1357
1358
1359
1360
1361
1362
1363
1364
1365
1366
1367
1368
1369
1370

Figure 4 – figure supplement 1. Estimating latent calcium - behavior correlations.

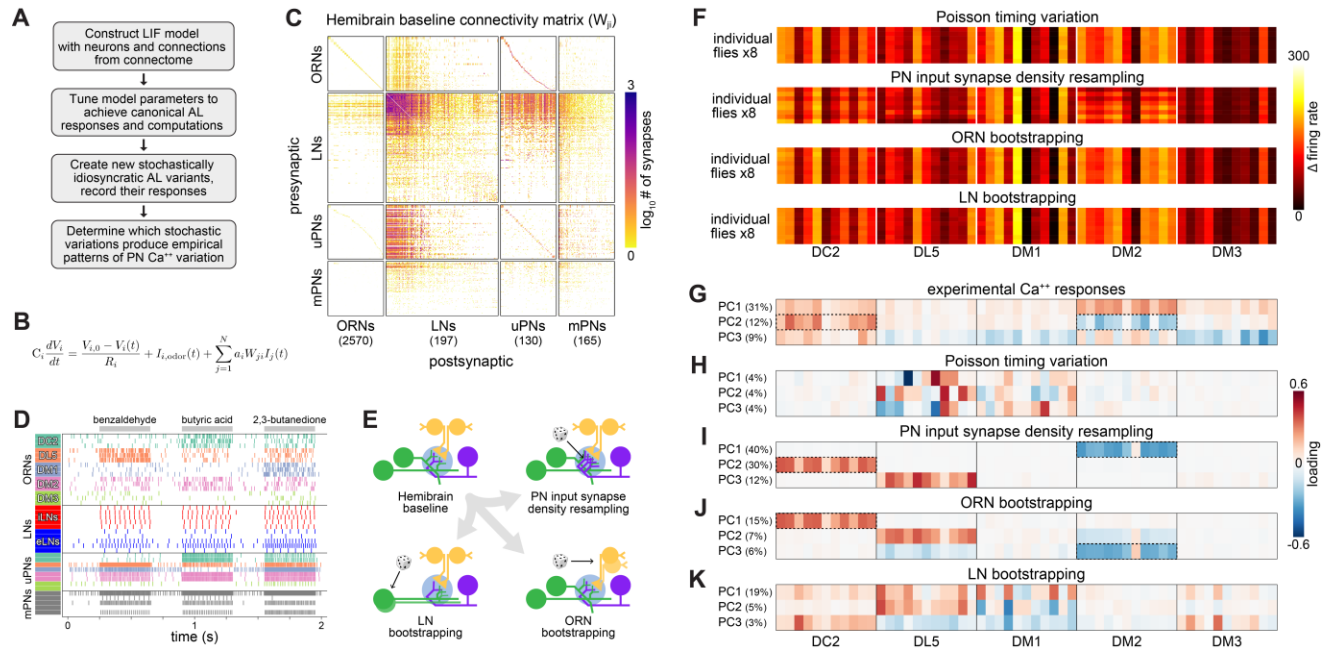
(A) Schematic of inference approach to estimate the correlation between latent calcium (c) and behavioral (b) states (ρ_{signal}). This method can be applied identically to infer ρ_{signal} between Brp measurements and behavior. (B) Demonstration of ρ_{signal} inference for OCT vs MCH models presented in Figure 4: ORN calcium PC 1 (left, $N=30$, $R^2=0.25$ indicated in dashed line), ORN Brp-Short PC 2 from trained model applied to train+test data (middle, $N=53$, $R^2=0.088$ indicated in dashed line), PN calcium PC 2 from trained model applied to train+test data (right, $N=69$, $R^2=0.20$). Black line indicates median $R_{c,b}^2$ ($R_{brp,b}^2$ for Brp-Short model) among the 10,000 simulations for each ρ_{signal} , shaded areas (from lightest to darkest to lightest) indicate 5-15th, 15-25th, ..., 85-95th percentile $R_{c,b}^2$ ($R_{brp,b}^2$). The marginal distribution for ρ_{signal} was estimated as the distribution of simulations for each ρ_{signal} for which the simulated $R_{c,b}^2$ ($R_{brp,b}^2$) had a value +/- 20% of the linear models' R^2 (dashed lines). For the examples depicted here, the median ρ_{signal} for ORN calcium PC1 was 0.30 (90% CI as estimated by the 5th-95th percentiles of the marginal distribution: 0.02-0.74), for ORN Brp-Short PC 2: 0.50 (0.11-0.85), for PN PC 2: 0.75 (0.44-0.96).



1371
1372
1373
1374
1375
1376
1377
1378
1379

Figure 4 – figure supplement 2. Time-dependent preference- and odor-decoding.

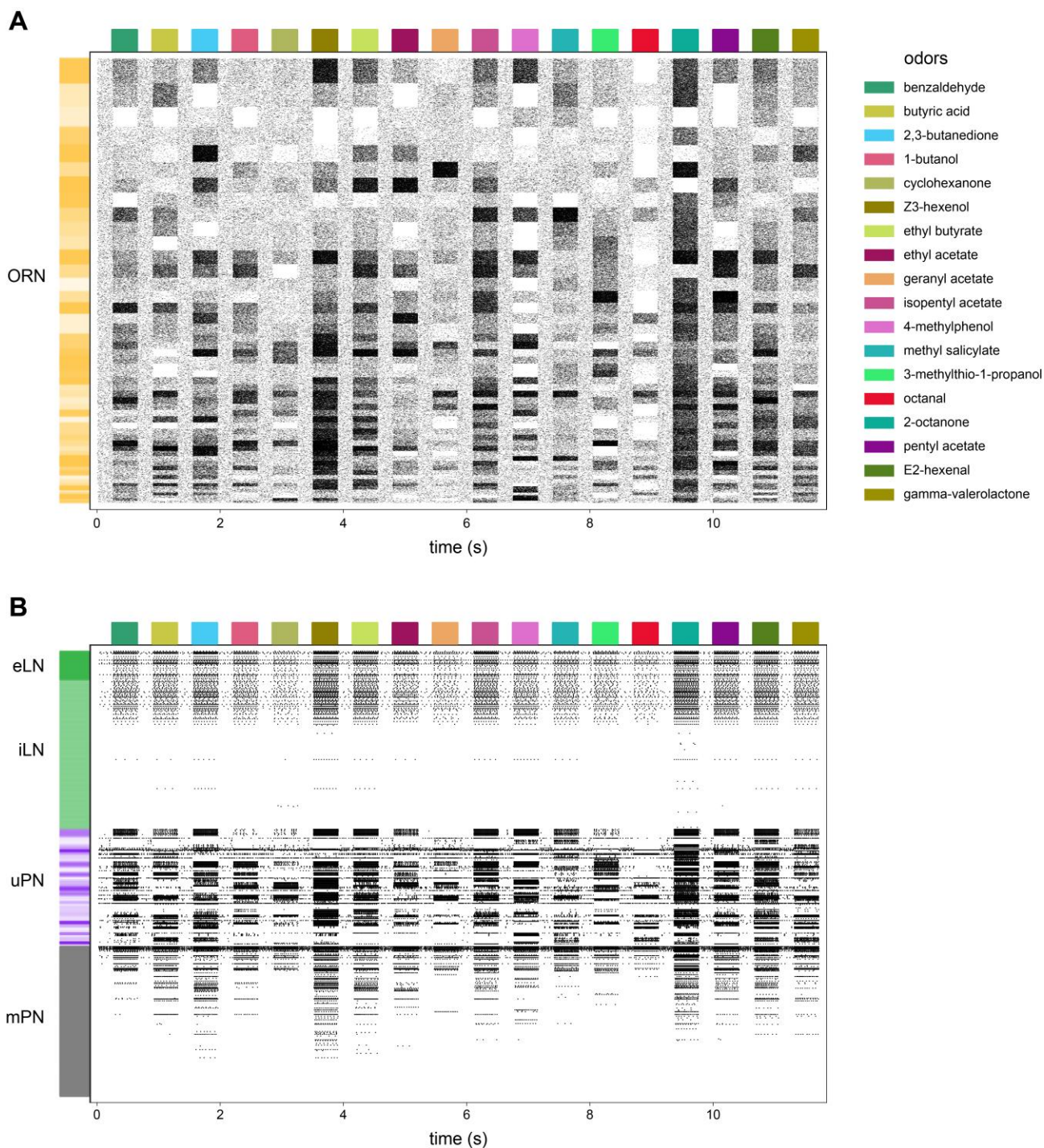
(A) R² of odor-vs-air preference predicted by PC 1 of PN activity as a function of time across trials (n=53 flies). (B) R² of odor-vs-air preference predicted by PC 1 of ORN activity as a function of time across trials (n=30 flies). (C) R² of odor-vs-odor preference predicted by PC 2 of PN activity (solid plum, n=69 flies) or PC 1 of ORN activity (dashed peach, n=35 flies) as a function of time across trials. (D) Logistic regression classifier accuracy of decoding odor identity from 5 glomerular responses as a function of time. Dashed curves indicate performance on shuffled data.



1380
 1381
 1382
 1383
 1384
 1385
 1386
 1387
 1388
 1389
 1390
 1391
 1392
 1393
 1394
 1395
 1396
 1397
 1398
 1399
 1400

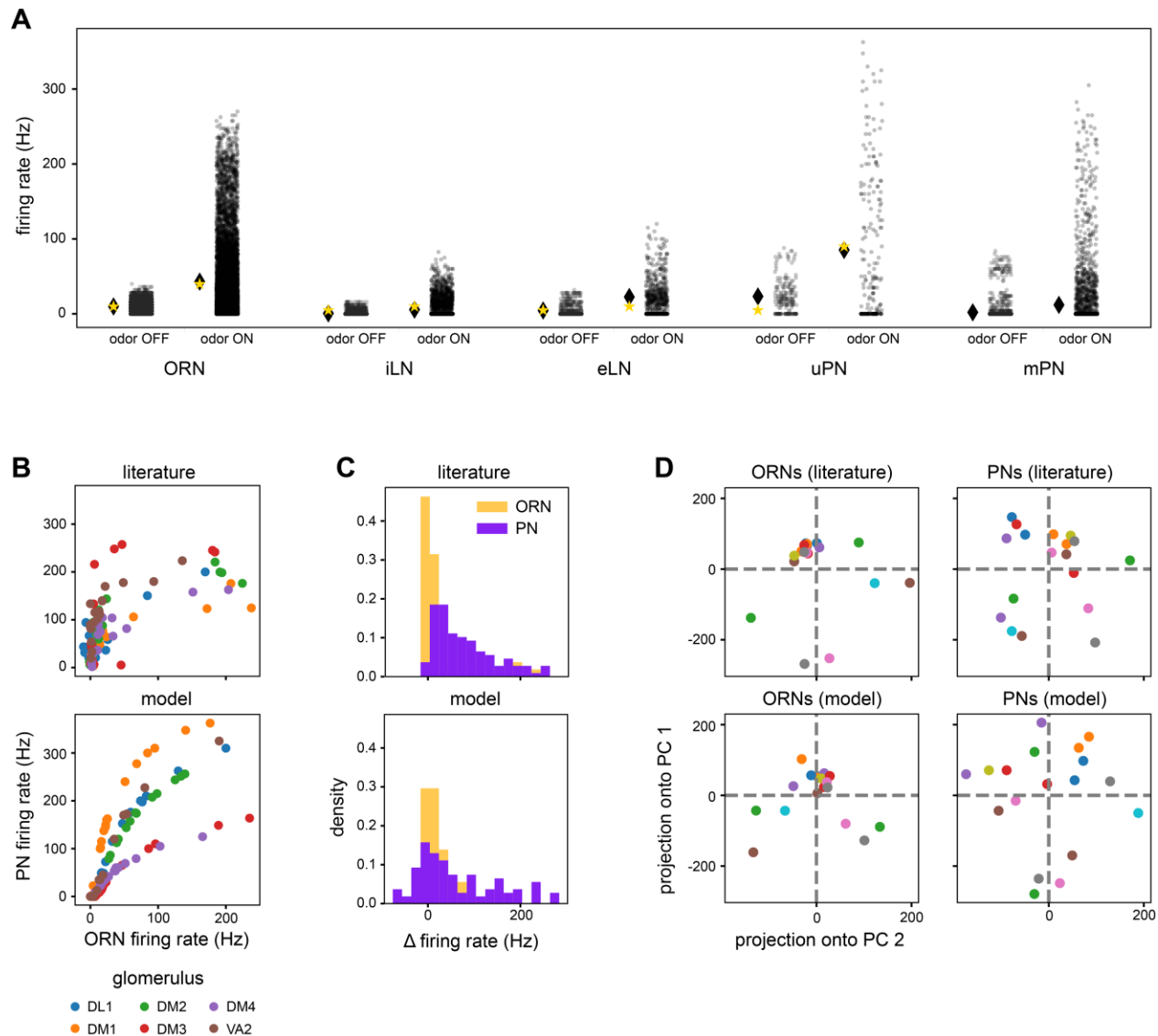
Figure 5. Simulation of developmentally stochastic olfactory circuits

(A) AL modeling analysis outline. (B) Leaky-integrator dynamics of each simulated neuron. When a neuron’s voltage reaches its firing threshold, a templated action potential is inserted, and downstream neurons receive a postsynaptic current. See *Antennal Lobe modeling* in Materials and Methods. (C) Synaptic weight connectivity matrix, derived from the hemibrain connectome (Scheffer et al., 2020). (D) Spike raster for randomly selected example neurons from each AL cell type. Colors indicate ORN/PN glomerular identity and LN polarity (i=inhibitory, e=excitatory). (E) Schematic illustrating sources of developmental stochasticity as implemented in the simulated AL framework. See Supplementary Video 4 for the effects of these resampling methods on the synaptic weight connectivity matrix. (F) PN glomerulus-odor response vectors for 8 idiosyncratic ALs subject to Input spike Poisson timing variation, PN input synapse density resampling, and ORN and LN population bootstrapping. (G) Loadings of the principal components of PN glomerulus-odor responses as observed across experimental flies (top). Dotted outlines highlight loadings selective for the DC2 and DM2 glomerular responses, which underlie predictions of individual behavioral preference. (H-K) As in (G) for simulated PN glomerulus-odor responses subject to Input spike Poisson timing variation, PN input synapse density resampling, and ORN and LN population bootstrapping. See Figure 5 – figure supplement 5 for additional combinations of idiosyncrasy methods. In (F-K) the sequence of odors within each glomerular block is: OCT, 1-hexanol, ethyl-lactate, 2-heptanone, 1-pentanol, ethanol, geranyl acetate, hexyl acetate, MCH, pentyl acetate and butanol.



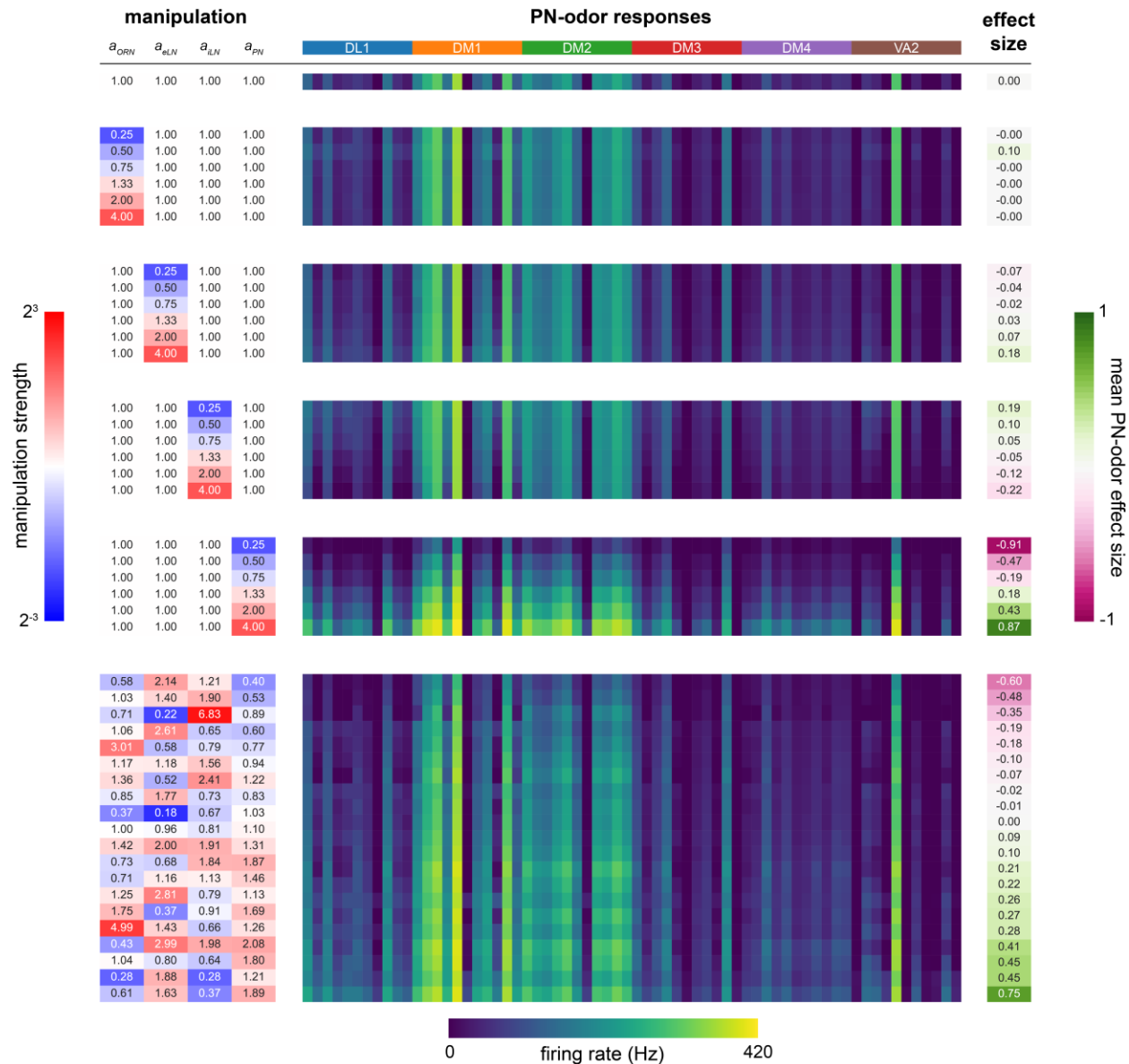
1401
1402 **Figure 5 – figure supplement 1. AL model raster plot.**

1403 (A) Action potential raster plot of ORNs in the baseline simulated AL. Rows are individual
1404 ORNs, black ticks indicate action potentials. Random shades of orange at left indicate blocks of
1405 ORN rows projecting to the same glomerulus. (B) The remaining neurons in the model. Shades
1406 of green indicate excitatory vs inhibitory LNs and shades of purple indicate PNs with dendrites
1407 in the same glomeruli.



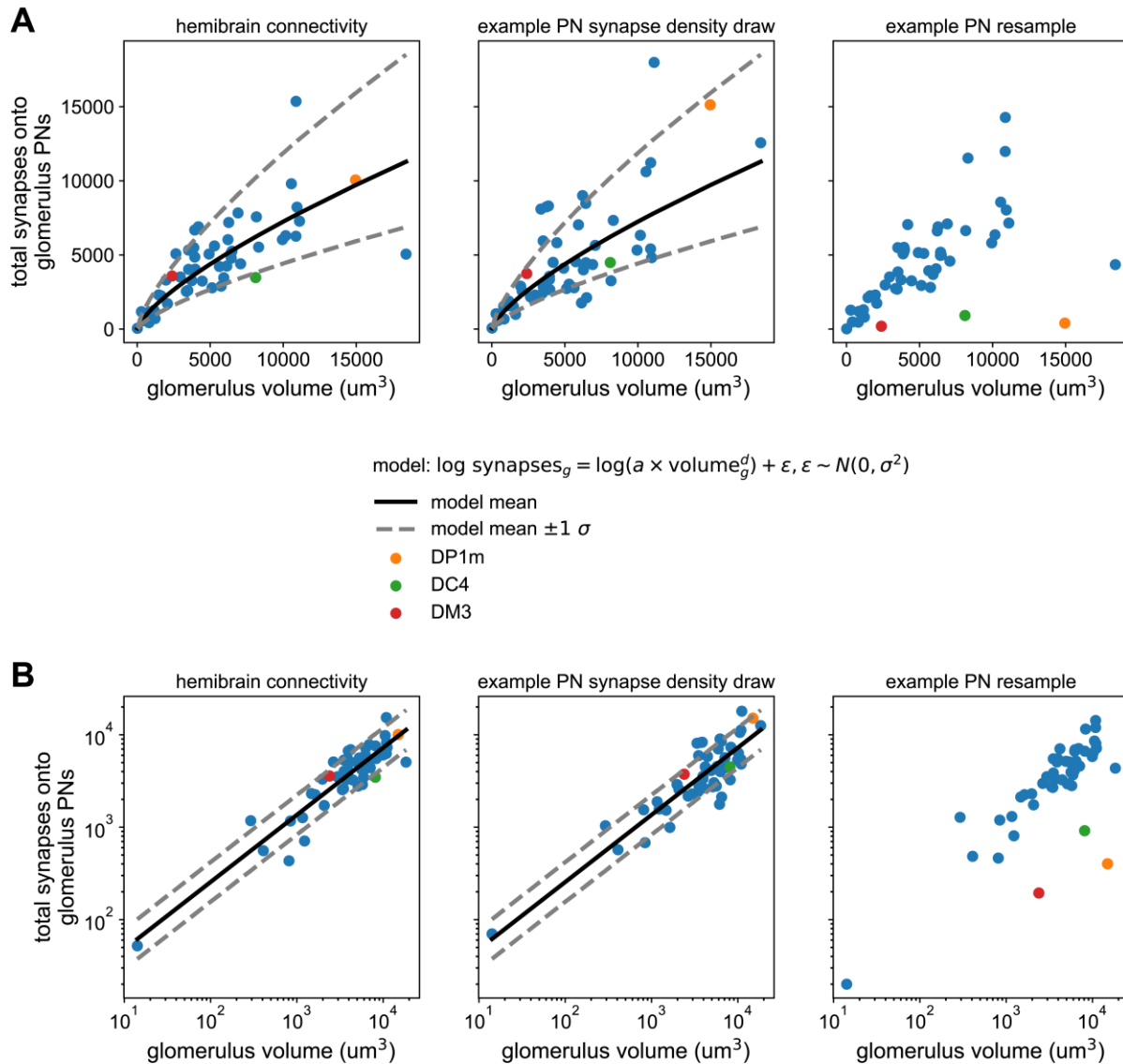
1408
1409
1410
1411
1412
1413
1414
1415
1416
1417
1418
1419
1420
1421
1422
1423
1424

Figure 5 – figure supplement 2. AL model baseline outputs compared to experimental data. (A) Distributions of model neuron firing rates by cell type across odors (transparent black points are individual neuron-odor combinations). Black lozenge symbols indicate the mean firing rate of the points to the right. Yellow stars indicate the comparable experimental values reported in (Chou et al., 2010; de Bruyne et al., 2001; Nagel et al., 2015; Wilson, 2004). (B) Scatter plots of average PN firing rate vs ORN firing rate during odor stimuli in the model vs experimental values (Bhandawat et al., 2007). Points are odors, colors are glomeruli. (C) Histograms of ON odor minus OFF odor glomerulus-average PN and ORN firing rates in the model vs experimental values (Bhandawat et al., 2007), showing flatter distributions in PNns. (D) Odor representations in the first 2 PCs of glomerulus-average ORN responses and PN responses in the model and experimental results (Bhandawat et al., 2007). Points are odors. Pairwise distances between PN representations are more uniform than in ORNs in both the model and experimental data. Panels (B)-(D) use glomerulus-average PN and ORN firing rates from six of the seven glomeruli in Bhandawat et al., 2007, as VM2 is significantly truncated in the hemibrain (Scheffer et al., 2020). Literature features in panels (B)-(D) were extracted from Bhandawat et al., 2007 using WebPlotDigitizer (Rohatgi, 2021).



1425 **Figure 5 – figure supplement 3. Sensitivity analysis of a_{ORN} , a_{eLN} , a_{iLN} , a_{PN} parameters.**
 1426 (Left, blue to red colormap): magnitude of parameter manipulation. (Center, dark blue to yellow
 1427 colormap): mean glomerular firing rate (Hz) responses of PNs (DL1, DM1, DM2, DM3, DM4,
 1428 VA2) to 11 odors (order within each glomerulus (colored bands at top): 3-octanol, 1-hexanol,
 1429 ethyl lactate, 2-heptanone, 1-pentanol, ethanol, geranyl acetate, hexyl acetate, 4-
 1430 methylcyclohexanol, pentyl acetate, 1-butanol, 3-octanol). (Right, pink to green colormap):
 1431 manipulation effect size on mean PN-odor responses (Cohen's d). (Top): baseline parameter set.
 1432 (Middle): single-parameter manipulations from 1/4x to 4x. (Bottom): multiple-parameter
 1433 manipulations. For further detail see *AL model tuning* in Materials and Methods. No
 1434 manipulations yielded effect sizes larger than 0.9; a_{PN} is the most sensitive parameter.
 1435

1436



1437

1438

1439

Figure 5 – figure supplement 4. Synapse counts vs glomerular volume in the hemibrain and AL model.

1440 (A) Left) Scatter plot of total PN input synapses within a glomerulus vs that glomerulus' volume

1441 from the hemibrain data set. Solid line represents the maximum likelihood-fit mean synapse

1442 count vs glomerular volume, and dashed lines the fit ± 1 standard deviation. Middle) As (left)

1443 but for a single sample from the parameterized distribution of PN input synapses vs glomerular

1444 volume. Right) As in previous for a single bootstrap resample of PNs. Color-highlighted

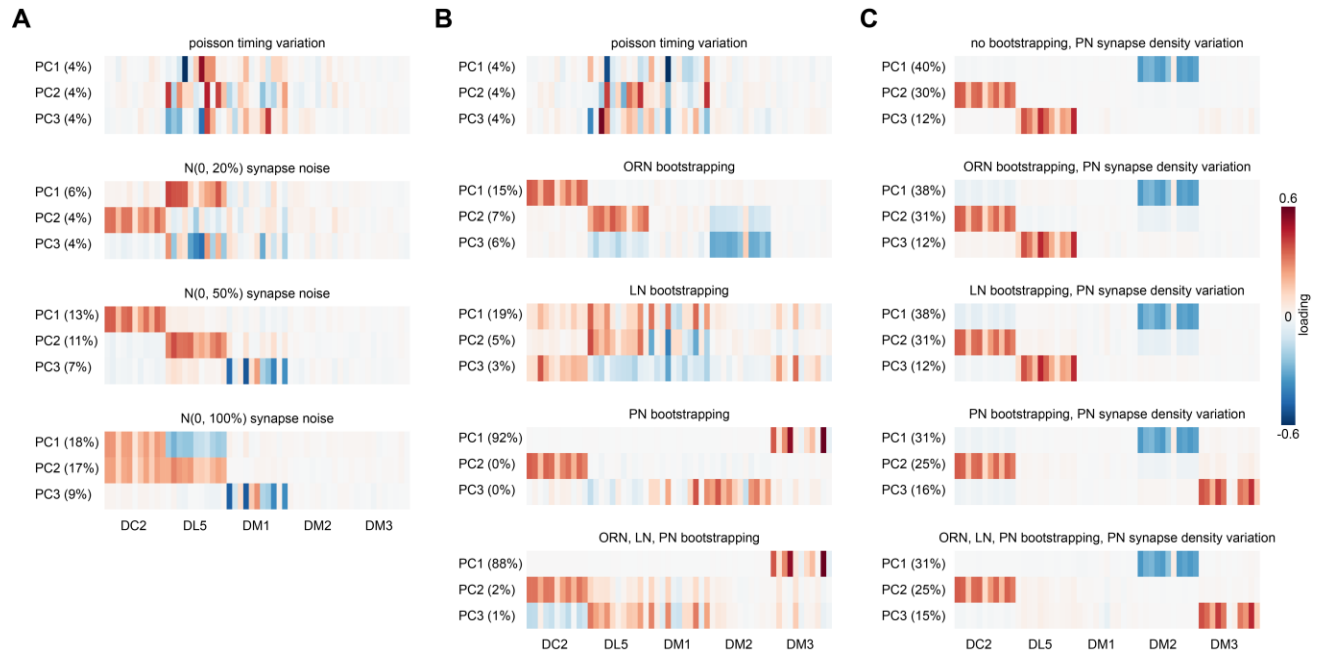
1445 glomeruli illustrate that when PNs within a glomerulus have highly asymmetrical synapse

1446 counts, bootstrapping them alone can result in apparent synapse densities that lie outside the

1447 empirical distribution (left). (B) As in (A) but on log-log axes, showing the linear relationship

1448 between synapse density and glomerular volume after this transformation, and bootstrapped

1449 densities falling outside this distribution at right.

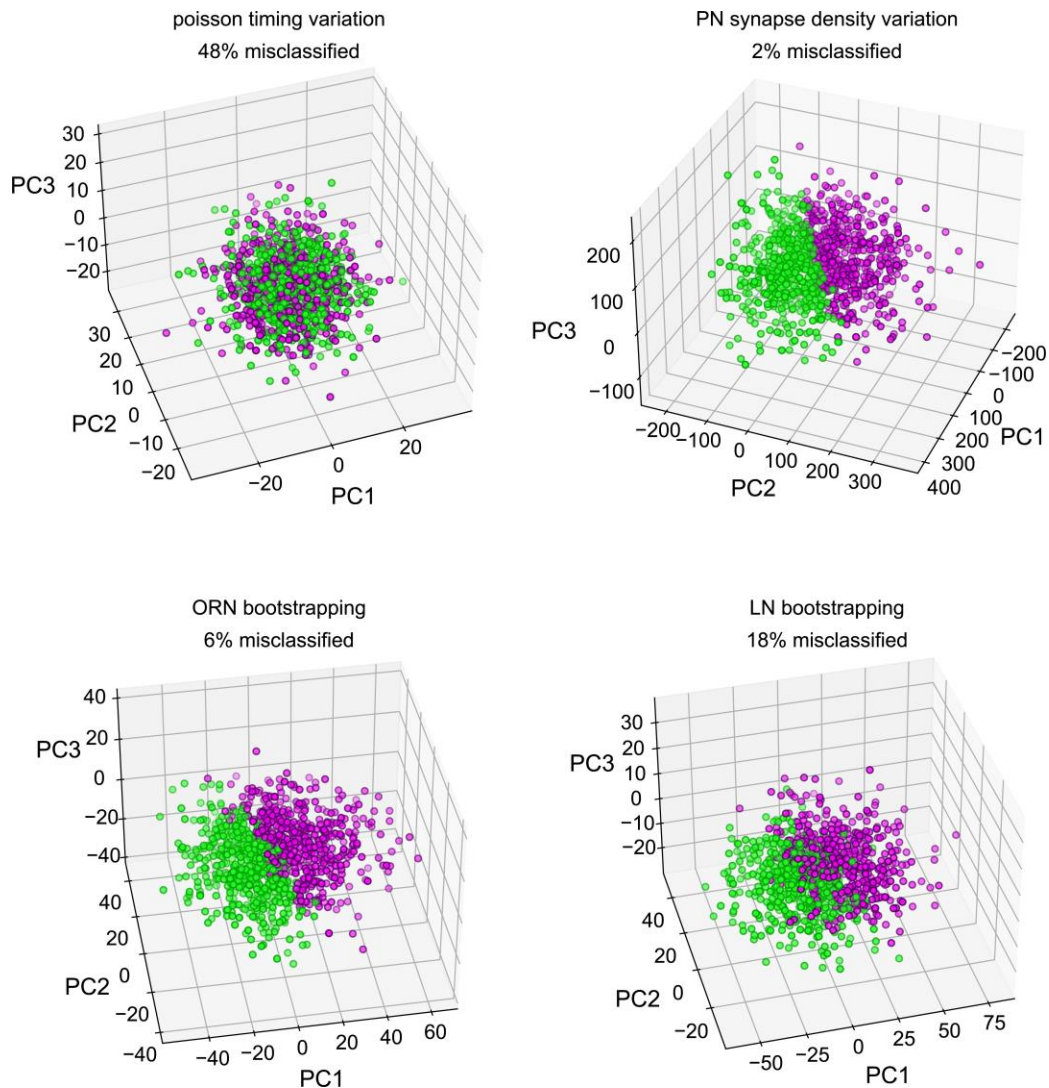


1450
1451
1452
1453
1454
1455
1456
1457
1458

Figure 5 – figure supplement 5. PN response PCA loadings under various sources of circuit idiosyncrasy.

(A) Loadings of the principal components of PN glomerulus-odor responses as simulated across AL models where Gaussian noise with a standard deviation equal to 0, 20, 50, and 100% of each synapse weight was added to each synaptic weight in the hemibrain data set. (B) circuit variation coming from bootstrapping of each major AL cell type or all three simultaneously. (C) circuit variation coming from bootstrap resampling of different cell-type combinations in addition to PN input synapse density resampling as illustrated in Figure 5 – figure supplement 4.

1459



1460

1461 **Figure 5 – figure supplement 6. Classifiability of simulated idiosyncratic behavior under**
1462 **different sources of circuit idiosyncrasy.**

1463 Simulated PN odor-glomerulus firing rates projected into their first three principal components.

1464 Individual points represent single runs of resampled AL models, under four different sources of

1465 idiosyncratic variation. PN responses in all odor-glomerulus dimensions were used to calculate

1466 simulated behavior scores for each resampled AL, by applying the PN calcium-odor-vs-odor

1467 linear model (Figure 2G). Magenta points represent flies with simulated preference for MCH in

1468 the top 50%, and green OCT preference. % Misclassification refers to 100% – the accuracy of a

1469 linear classifier trained on MCH-vs-OCT preference in the space of the first three PCs. This

1470 measures how much of the variance along the PN calcium-odor-vs-odor linear model lies outside

1471 the first three PCs of simulated PN variation.

1472 **Tables**

1473

1474 **Table 1: Calcium & Brp-Short – behavior model statistics**

Behavior Measured	Neural Predictor	Figure Panel	n	β_0	β_1	R ²	p-value
OCT vs. AIR	PN Calcium PC 1 (Figure 2A)	Figure 2 – figure supplement 1A	18	-0.26	-0.079	0.16	0.099
OCT vs. AIR	PN Calcium Average all dimensions	2C	53	-0.051	-0.38	0.098	0.022
OCT vs. AIR	ORN Calcium PC 1 (Figure 2D)	1L	30	-0.29	-0.053	0.23	0.007
OCT vs. AIR	ORN Calcium Average all dimensions	2F	30	-0.032	-0.71	0.25	0.005
OCT vs. MCH	PN Calcium PC 2 (Figure 2G)	Figure 2 – figure supplement 1C	47	-0.058	-0.081	0.15	0.006
OCT vs. MCH	PN Calcium DM2 - DC2 (% difference)	2I	69	-0.032	-0.0018	0.12	0.004
OCT vs. MCH	ORN Calcium PC 1	1O	35	-0.14	-0.027	0.031	0.32
OCT vs. MCH	ORN Brp-Short PC 2 (train data only) (Figure 3E)	Figure 3 – figure supplement 1I	22	-0.087	0.017	0.22	0.028
OCT vs. MCH	ORN Brp-Short PC 2 (all data)	3F	53	-0.019	0.012	0.088	0.031
OCT vs. MCH	ORN Brp-Short DM2 - DC2	3G	53	-0.051	-0.007	0.053	0.096

1475

1476 **Table 2: Typical electrophysiology features of AL cell types, used as model parameters**

Parameter	ORNs	LN _s	PN _s
Membrane resting potential	-70 mV (Dubin and Harris, 1997)	-50 mV (Seki et al., 2010)	-55 mV (Jeanne and Wilson, 2015)
Action potential threshold	-50 mV (Dubin and Harris, 1997)	-40 mV (Seki et al., 2010)	-40 mV (Jeanne and Wilson, 2015)
Action potential minimum	-70 mV (Cao et al., 2016)	-60 mV (Seki et al., 2010)	-55 mV (Jeanne and Wilson, 2015)
Action potential maximum	0 mV (Dubin and Harris, 1997)	0 mV (Seki et al., 2010)	-30 mV (Wilson and Laurent, 2005)
Action potential duration	2 ms (Jeanne and Wilson, 2015)	4 ms (Seki et al., 2010)	2 ms (Jeanne and Wilson, 2015)
Membrane capacitance	73 pF (assumed = PN _s)	64 pF (Huang et al., 2018)	73 pF (Huang et al., 2018)
Membrane resistance	1.8 GOhm (Dubin and Harris, 1997)	1 GOhm (Seki et al., 2010)	0.3 GOhm (Jeanne and Wilson, 2015)

1477

1478 **Supplementary Videos**

1479

1480 **Supplementary Video 1. Example recording with automated tracking of an odor-vs-air**
1481 **behavioral assay.**

1482 The recent positions of each fly (green line) are shown in different colors. Red bar indicates
1483 when the odor stream is turned on.

1484

1485 **Supplementary Video 2. Example recording with automated tracking of an odor-vs-odor**
1486 **behavioral assay.**

1487 The recent positions of each fly (green line) are shown in different colors. Magenta and green
1488 bars at right indicate when MCH and OCT are respectively flowing into the top and bottom
1489 halves of each arena.

1490

1491 **Supplementary Video 3. Confocal image stack of expanded DC2>Brp-Short.**

1492 Magenta is nc82 stain, Green is Or13a>Brp-Short. Frames are z-slices spaced at 0.54 μm . Image
1493 height corresponds to a post-expansion field of view of 107 x 90 μm (a ~ 2.5 x linear expansion
1494 factor).

1495

1496 **Supplementary Video 4. Simulated AL connectivity matrices.**

1497 Left: Glomerular density resampling. Each frame corresponds to the hemibrain connectome
1498 synaptic weights, rescaled according to a sample from the relationship between synapse count
1499 and volume parameterized in Figure 5 – figure supplement 4. Middle: ORN bootstrapping. Each
1500 frame corresponds to the hemibrain connectome synaptic weights, but with the population of
1501 ORNs projecting to each glomerulus resampled with replacement. Right: LN bootstrapping.
1502 Each frame corresponds to the hemibrain connectome synaptic weights, but with the population
1503 of LNs resampled with replacement.